The Invading Anchor Cell Induces Lateral Membrane Constriction during Vulval Lumen Morphogenesis in C. elegans

Yang, Qiutan ; Roiz, Daniel ; Mereu, Louisa ; Daube, Michael ; Hajnal, Alex

Abstract: During epithelial tube morphogenesis, linear arrays of cells are converted into tubular structures through actomyosin-generated intracellular forces that induce tissue invagination and lumen formation. We have investigated lumen morphogenesis in the C. elegans vulva. The first discernible event initiating lumen formation is the apical constriction of the two innermost primary cells (VulF). The VulF cells thereafter constrict their lateral membranes along the apicobasal axis to extend the lumen dorsally. Lateral, but not apical, VulF constriction requires the prior invasion of the anchor cell (AC). The invading AC extends actin-rich protrusions toward VulF, resulting in the formation of a direct AC-VulF interface. The recruitment of the F-BAR-domain protein TOCA-1 to the AC-VulF interface induces the accumulation of force-generating actomyosin, causing a switch from apical to lateral membrane constriction and the dorsal extension of the lumen. Invasive cells may induce shape changes in adjacent cells to penetrate their target tissues.

DOI: https://doi.org/10.1016/j.devcel.2017.07.008

The invading anchor cell induces lateral membrane constriction during vulval lumen morphogenesis in *C. elegans*

Qiutan Yang[1,2], Daniel Roiz[1,2], Louisa Mereu[1,2], Michael Daube[1], Alex Hajnal[1,3]

[1]University of Zurich, Institute of Molecular Life Sciences, Winterthurerstrasse 190 CH-8057 Zurich, Switzerland.

[2]Zurich PhD Program in Molecular Life Sciences

[3]corresponding author and lead contact: alex.hajnal@imls.uzh.ch

Keywords: *Caenorhabditis elegans*, morphogenesis, lumen formation, actomyosin, Bin–Amphiphysin–Rvs domain, cell invasion.

running title: Cell invasion during lumen morphogenesis

09.07.17

SUMMARY

During epithelial tube morphogenesis, linear arrays of cells are converted into tubular structures through actomyosin generated intracellular forces that induce tissue invagination and lumen formation. We have investigated lumen morphogenesis in the *C. elegans* vulva. The first discernible event initiating lumen formation is the apical constriction of the two inner-most primary cells (VulF). The VulF cells thereafter constrict their lateral membranes along the apico-basal axis to extend the lumen dorsally. Lateral but not apical VulF constriction requires the prior invasion of the anchor cell (AC). The invading AC extends actin-rich protrusions towards VulF, resulting in the formation of a direct AC-VulF interface. The recruitment of the F-BAR domain protein TOCA-1 to the AC-VulF interface induces the accumulation of force-generating actomyosin, causing a switch from apical to lateral membrane constriction and the dorsal extension of the lumen. Invasive cells may induce shape changes in adjacent cells to penetrate their target tissues.

INTRODUCTION

Tubes are the basic building blocks of most epithelial organs (Andrew and Ewald, 2010; Lubarsky and Krasnow, 2003). A key step during the morphogenesis of tubular organs is the invagination of the tissue, which converts a monolayer of epithelial cells into a three-dimensional structure. The constriction of the apical cell surface is a crucial process that initiates the bending of the invaginating epithelium. Apical constriction has been extensively studied, most notably during gastrulation, vertebrate neurulation, dorsal closure in *Drosophila* and branching morphogenesis of various tubular organs (Sawyer et al., 2010). In all of these examples, apical constriction is the result of contractile forces generated by the actomyosin network on the apical cortex of the cells. These cell shape changes can either be controlled by cell intrinsic factors or by extracellular cues such as diffusible growth factor signals. In particular, during gastrulation cell intrinsic transcription factors that determine the regional cell fates induce apical constriction in the invaginating epithelium, while fibroblast and vascular endothelial growth factors (FGF and VEGF) released from neighboring cells induce apical constriction during branching morphogenesis of tubular organs (Helker et al., 2013). In all of these cases, apical constriction is induced through intracellular signaling pathways that control actomyosin contractility, via a CDC-42 or Rho-dependent kinase that phosphorylates and thereby activates the non-muscle myosin light chain regulatory subunit (Heisenberg and Bellaiche, 2013). The sub-cellular localization and orientation of the actomyosin network plays a pivotal role in determining the directivity and distribution of the intracellular forces between the different cortical domains. Hence, the localized activation of the various actomyosin regulators determines the type of shape changes a cell will undergo.

In this study, we have investigated the cell shape changes occurring during lumen morphogenesis in the *C. elegans* vulva, the egg-laying organ of the hermaphrodite. The vulva is a tubular organ that passes the fertilized eggs from the uterus to the outside. Thanks to the small number of only 22 cells that form the vulval tube and to the ability to observe the process in real time, vulval development is an excellent model to study epithelial morphogenesis at single cell resolution (Schindler and Sherwood, 2012). Vulval invagination and lumen formation begins in L3 larvae, after the three proximal vulval precursor cells (VPCs), P5.p, P6.p and P7.p, have each divided twice to generate 12 vulval cells (Fig. 1A). At this stage, the gonadal anchor cell (AC), which is located dorsally to the vulval cells, has breached the two basal laminae separating the gonad from the vulva (Sherwood and Sternberg, 2003). Thereafter, the AC invades the vulval epithelium

and establishes direct cell-cell contacts with the two inner-most primary (1°) VulF cells. The VulF cells then begin to move dorsally and initiate the formation of the vulval lumen (Fig. 1A). The remaining vulval cells (VulE through VulA) follow the VulF cells while undergoing their last round of cell divisions. After these cell rearrangements, the vulval tube is formed by a stack of seven toroids that are each generated by the homotypic fusion between vulval cells of the same subfate (Schindler and Sherwood, 2012). Whereas the molecular pathways controlling vulval fate specification and AC invasion are well studied, the events that initiate the formation of the vulval lumen have not yet been characterized. In particular, it is unknown what type of cell-cell interactions and signaling pathways control the cell shape changes that are required for wild-type lumen morphogenesis.

We have used live-imaging combined with cell ablation experiments and cortical tension measurements to dissect the temporal sequence of events occurring during vulval lumen morphogenesis. In contrast to other known models of lumen formation, vulval lumen morphogenesis involves a sequence of apical and lateral membrane constrictions of the VulF cells, which extend the lumen dorsally. The invading AC plays a central role in orchestrating the vulval cell shape changes. The newly forming AC-VulF interface reorganizes the cortical actomyosin network in the VulF cells and induces the constriction of the VulF cells along their lateral membranes, after apical constriction has been completed. For this purpose, the F-BAR (Bin-Amphiphysin-Rvs) domain protein TOCA-1 (Bai and Grant, 2015) is recruited to the AC-VulF contact sites. TOCA-1 and its paralog TOCA-2 then capture the non-muscle myosin NMY-2 to reorient the contractile forces in the VulF cells along the dorso-ventral axis. In this manner, the temporal sequence of cell autonomous apical and AC-induced lateral membrane constriction shapes the vulval lumen.

RESULTS

Sequential apical and lateral constriction of the VulF cells during vulval lumen morphogenesis

The formation of the vulval lumen begins after the second round of vulval cell divisions in mid L3 larvae (Pn.pxx stage). First, the apical membranes of two inner descendants of P6.p (the VulF cells P6.pap and P6.ppa) detach from the cuticle and the cells move dorsally (Fig. 1A,B). As the vulval lumen gradually expands, the vulval cells undergo their last round of cell divisions to generate 22 cells with seven different subfates (the 1° VulF and VulE cells and the 2° VulD through VulA cells) that form the vulval tube (Sharma-Kishore et al., 1999).

We characterized the cell shape changes during the early phases of vulval lumen morphogenesis by performing 3D time-lapse microscopy of mid to late L3 larvae. For this purpose, we first observed larvae expressing the CED-10::GFP reporter, which labels the basolateral plasma membranes (Lundquist et al., 2001). Before the emergence of a lumen, the apical VulF membranes began to constrict, resulting in a gradual shortening of the distance between the apical ends of their lateral membranes (40 minute time point in Fig. 1B-B'', suppl. Movie S1 and suppl. Fig. S1A for quantification). The VulE and the 2° cells, on the other hand, did not display signs of apical constriction at this stage. Around the time when the apical constriction of VulF had reached its maximum, the VulE cells underwent their last round of transversal (along the left/right axis) divisions (100 minute time point in Fig. 1B-B''), making space for VulD to move towards the vulval midline and establish direct contact with VulF (140 minute time point in Fig. 1B-B'',C'). After the VulE divisions, the apical VulF membranes relaxed partially, while the lateral membranes between the two VulF cells started to constrict until their apical ends reached the basal apex of the VulF cells, a process we termed lateral constriction (200 minute time point in Fig. 1B-B'', suppl. Movie S1 and suppl. Fig. S1B for quantification). After the lateral constriction had been completed, the VulF cells underwent their last round of divisions. This temporal sequence of apical and lateral VulF membrane constrictions separated by the VulE divisions resulted in the formation of a characteristic pointed vulval lumen that extends to the AC-VulF contact sites (last time point in Fig. 1B-B'').

The invading AC extends dynamic protrusions towards the apical VulF junctions

Prior to vulval lumen formation, the gonadal AC breaches the two basal laminae that separate the vulval epithelium from the uterus and invades the vulval tissue (Sherwood and Sternberg, 2003). We investigated the morphology of the AC during vulval lumen formation after basal laminae breaching had occurred. For this purpose, we observed lumen formation in animals carrying the $P_{cdh\text{-}3}$*>mCherry::PLCδ*^{PH} reporter, which labels the phosphatidylinositol-4,5-bisphosphate (PIP_2) containing actin-rich AC plasma membranes, along with the apical junction (AJ) marker $P_{ajm\text{-}1}$*>ajm-1::gfp* (Ziel et al., 2009). As the VulF cells underwent apical constriction, the AC extended circumferential actin-rich protrusions that were directed at the AJs between the two VulF cells (suppl. Movie S2, Fig. 1C-C''). After VulE division and during lateral VulF constriction, the AC protrusions gradually retracted dorsally (compare third and fifth panels in Fig. 1C'') until the VulF AJs were bent forming an arch underneath the AC body (fifth panel in Fig. 3C, see 3D reconstruction in suppl. Movie S3). As a result of these cell shape changes, a junction between the AC and the VulF cells was formed (arrowhead in the fifth panel of Fig. 1C'').

The extension of dynamic AC protrusions towards the VulF AJs suggested an active role of the AC in inducing the vulval cell shape changes during lumen formation. The AC protrusions may, for example, guide the apical VulF junctions to move dorsally during lateral membrane constriction.

The AC induces lateral VulF constriction

To test if the AC regulates the shape changes of the vulval cells, we examined the requirement for direct contact formation between VulF and the AC. For this purpose, we observed the *fos-1(ar105)* mutant, in which the AC does not breach the basal laminae and the AC protrusions can not reach the AJs of the VulF cells (Sherwood et al., 2005). *fos-1(ar105)* mutants did not exhibit any signs of lateral VulF constriction, while apical constriction was not significantly affected (Fig. 2A,B and suppl. Fig. S1 for quantification). To distinguish if the absence of basal laminae breaching or the lack of cell-cell contact *per se* caused the loss of lateral VulF constriction, we ablated the AC at the mid-Pn.pxx stage, after the basal laminae had been breached but before the onset of lumen formation. Similar to *fos-1(ar105)* mutants, AC ablation after basal laminae breaching resulted in the absence of lateral VulF constriction (Fig. 2C and suppl. Fig. S1 for quantification). In both, AC ablated animals and *fos-1(ar105)* mutants, we noticed a slight delay in vulval lumen formation. For example, in the AC ablated animal shown in Fig. 2C no lumen was

detectable at the 230 minutes time point, even though both VulF cells had initiated their last round of divisions.

We conclude that AC invasion, which permits the formation of direct AC-VulF contact, is required to induce lateral VulF membrane constriction. Apical VulF constriction, on the other hand, does not depend on direct contact with the AC and hence appears to be an intrinsic property of the 1° VulF cell fate. In the absence of lateral VulF constriction, a vulval lumen does form, though at a slower rate and the lumen is not extended dorsally to reach the AC.

Accumulation of the actomyosin network at the AC-VulF contact sites

Contractile forces generated by the actomyosin network induce epithelial cell shape changes in many developmental processes, including apical constriction during *C. elegans* gastrulation (Sawyer et al., 2010). We thus examined the subcellular localization of the actomyosin network during vulval lumen formation. To visualize actin filaments (F-actin), we used the $P_{dlg\text{-}1}$*>LifeAct::gfp* reporter (Farooqui et al., 2012). During apical and lateral VulF constriction, most of the F-actin signal in the 1° cells was detected on the basolateral cortex and adjacent to the AJs (Fig. 3 A) (Haag et al., 2014). 3D image reconstructions of the VulF cells during lateral constriction revealed a ring-shaped pattern of F-actin staining on the lateral VulF cortex (Fig. 3A', quantified in E).

To observe myosin localization, we performed 3D time-lapse recordings of an endogenous reporter for non-muscle myosin II (NMY-2::GFP) along with the $P_{cdh\text{-}3}$*>mCherry::PLC*δ^{PH} AC marker (Fig. 4A, suppl. Movie S6) (Dickinson et al., 2013). Prior to lumen formation, NMY-2::GFP was predominantly localized near the AJs between the vulval cells. However, during lateral constriction the NMY-2::GFP signal became enriched on the basal side of the VulF cells at the AC-VulF contact sites (arrowheads in Fig. 4A,C,C', quantified in J). Similar to the cells undergoing apical constriction during gastrulation in the embryo (Nance et al., 2005), NMY-2::GFP exhibited a highly dynamic pattern with distinct punctae moving along the VulF membranes (suppl. Movie S6). We performed particle tracking on mid-sagittal sections taken at one-second time intervals to estimate the speed of the of NMY-2::GFP punctae in the VulF cells (suppl. Fig. S2). This analysis revealed that the movement of NMY-2::GFP punctae, which had reached the AC-VulF contact sites, was significantly slower compared to punctae on the basolateral VulF membranes at a distance from the AC (Fig. 4B).

Taken together, the subcellular distribution of the F-actin network and the dynamic movement of NMY-2 in the VulF cells undergoing lateral constriction suggested that contractile forces are generated not only on the apical cortex but also at the contact sites between the AC and the VulF cells.

Apical mislocalization of the actomyosin network and lumen morphogenesis defects

To further test the relative contributions of the basolateral and apical actomyosin pools to lumen morphogenesis, we examined *erm-1* mutants (Van Fürden et al., 2004). *erm-1* encodes a member of the Ezrin/Radixin/Moesin (ERM) protein family that is required for basolateral F-actin localization in the vulval cells (Haag et al., 2014). *erm-1(tm677)* null mutants exhibited a reduction in basolateral and a concomitant increase in apical F-actin staining in all vulval cells at the Pn.pxx stage (Fig. 3B). In particular, no ring-shaped F-actin staining could be observed on the lateral VulF cortex of *erm-1(tm677)* mutants (Fig. 3B',E). We next examined if the apical mislocalization of F-actin in *erm-1(lf)* mutants affected NMY-2 distribution. Since the *erm-1* and *nmy-2* genes are located in close proximity on LGI, we used *erm-1* RNAi to observe if reducing *erm-1* expression altered NMY-2::GFP localization. RNAi knock-down of *erm-1* caused a strong reduction in NMY-2::GFP accumulation at the AC-VulF contact sites in the affected animals (42% affected, n=71) (Fig. 4D,D',J). Moreover, time-lapse microscopy using a CED-10::GFP reporter revealed a characteristic lumen morphogenesis defect in *erm-1(tm677)* mutants. Instead of extending the lumen dorsally, the lumen in *erm-1(tm677)* mutants had a bulged shape and did not reach the AC-VulF contact sites (Fig. 2D,D' and suppl. Movies S4, S5). Lateral VulF constriction did not occur in *erm-1(tm677)* mutants, while apical VulF constriction was increased when compared to wild-type larvae (suppl. Fig. S1 for quantification).

These results indicated that the apical mislocalization of the actomyosin network in the VulF cells leads to the loss of lateral VulF constriction and an abnormal lumen morphogenesis. We thus conclude that a balance between apical and basolateral actomyosin-driven membrane constrictions is necessary to shape the vulval lumen.

Cortical tension measurements on the lateral and apical VulF cortex

The results presented so far suggested that a contractile force on the lateral VulF cortex is an important factor in determining the shape of the vulval lumen. To directly test this

hypothesis, we measured the cortical tension in the different compartments of the VulF cells during apical and lateral constriction by performing laser nanosurgery experiments with a pulsed two-photon infrared laser (see materials and methods) (Mayer et al., 2010) and Vuong and Labouesse, personal communication). During lateral VulF constriction in wild-type animals, we observed a rapid recoil after cutting across the middle section of the lateral VulF cortex (Fig. 5A). By contrast, a significantly smaller recoil was observed in *erm-1(tm677)* mutants at the same developmental stage, indicating a reduced actomyosin-generated tension on the lateral cortex (Fig. 5A,B). We also measured the cortical tension generated during apical constriction before the onset of lumen formation (Fig. 5C,D). This experiment revealed a slight increase in the apical membrane tension in *erm-1(tm677)* mutants compared to wild-type larvae at the same stage, which might reflect the increased F-actin concentration on the apical VulF cortex in *erm-1(tm677)* mutants.

Finally, we investigated the consequences of cutting across the lateral VulF membranes by observing lumen formation in animals that had undergone laser nanosurgery. As negative control, we examined animals, in which the lateral membranes between the distal VulA and VulB cells had been cut (Fig 5E). Lumen formation in animals that recovered from this intervention and repaired the cut site (seen by the reappearance of the CED-10::GFP signal with a small scar remaining on the lateral membrane) was scored around 4 hours later, after the subsequent division of the VulE cells. In the animals cut across the lateral VulF cells, lateral membrane constriction was reduced, and an abnormal lumen was formed in all cases (Fig 5E, quantified in F). By contrast, the control animals that were cut across the lateral VulA/B membranes underwent complete lateral VulF constriction and formed a normal lumen (Fig 5E,F).

In conclusion, the cortical tension measurements support the notion that the basolateral actomyosin network generates a contractile force to cause lateral VulF constriction during lumen morphogenesis.

The invading AC reorients the actomyosin network in the VulF cells

We next examined the localization of the actomyosin network in mutants defective in AC invasion. In *fos-1(ar105)* mutants, the NMY-2::GFP signal at the VulF-AC contact sites was reduced and distributed in irregular patches along the basal VulF and VulE cortex (Fig. 4E,E',J). Also, the ring-shaped F-actin staining on the lateral VulF membrane was perturbed (Fig. 3C,C',E). To test if the polarity of the AC is required for the reorganization of the actomyosin network in the VulF cells, we examined *unc-6(ev600)* loss-of-function

mutants. *unc-6* encodes a Netrin homolog that functions as a guidance signal from the ventral nerve cord neurons by polarizing the invading AC towards the ventral side (Ziel et al., 2009). In the absence of the UNC-6 Netrin guidance signal, no actin-rich protrusions towards the VulF cells are produced and the AC is often misplaced. Similar to *fos-1* mutants, the accumulation of NMY-2::GFP at the AC-VulF contact sites and the ring-shaped F-actin staining were lost in *unc-6(ev400)* mutants (Fig. 4F,F',J and Fig. 3D,D',E), indicating that the formation of AC protrusions is necessary to reorganize the actomyosin network in the VulF cells. Furthermore, tracking of the NMY-2::GFP punctae in *unc-6(ev600)* mutants indicated that the mobility of NMY-2 punctae at the basal apex of the VulF membranes remains high if no contact is made with the AC (Fig. 4B and suppl. Fig. S2).

Next, we tested whether NMY-2::GFP is recruited to the contact sites in both the AC and VulF cells or if the invading AC induces NMY-2::GFP accumulation exclusively in the VulF cells. For this purpose, we performed tissue-specific *nmy-2* RNAi knock-down using the *qyIs102[fos-1::rde-1(+)]*(Matus et al., 2010) and *mfIs70[lin-31::rde-1(+)]*(Barkoulas et al., 2013), transgenes in the *nmy-2::gfp; rde-1(lf); rrf-3(lf)* background to induce AC-specific and VPC-specific RNAi, respectively. Upon VPC-specific *nmy-2* RNAi, the accumulation of NMY-2::GFP at the AC-VulF contact sites was strongly reduced in all 22 affected animals (Fig. 4G,H). By contrast, AC-specific *nmy-2* RNAi did not affect the recruitment of NMY-2::GFP to the AC-VulF interface in 11 out of 13 affected animals (Fig. 4G',H'). Though, in two animals NMY-2::GFP accumulation at the AC-VulF contact sites was partially reduced, possibly due to perturbed AC invasion (not shown). Moreover, 1° vulval lineage-specific expression of NMY-2::GFP using the *egl-17* promoter (Burdine et al., 1998) was sufficient to cause NMY-2::GFP recruitment to the AC-VulF contact sites (Fig. 4I-I'').

We conclude that NMY-2 accumulation at the AC-VulF contact sites occurs predominantly in the VulF cells. Thus, the invading AC reorganizes the actomyosin network in the VulF cells, resulting in a switch from apical to lateral VulF membrane constriction.

Recruitment of the F-BAR domain protein TOCA-1 during lateral VulF constriction

We noticed that prior to lateral membrane constriction the invading AC deformed the lateral membranes of the VulF cells at their basal apex, resulting in a basal membrane indentation (see arrowhead in Figure 3A and suppl. Movie S7 for a 3D reconstruction). By contrast, the VulF cells In *fos-1(ar105)* mutants, in which the AC does not breach the basal

laminae, or in AC-ablated animals were not deformed on their basal side (compare the VulF cell shapes in Figure 2A' versus B',C'). We thus hypothesized that the membrane deformation of the VulF cells caused by the invading AC constitutes a signal that induces the reorganization of the actomyosin network during lateral membrane constriction. Proteins containing an N-terminal Bar (Bin-Amphiphysin-Rvs) domain bind to curved plasma membranes and activate Rho family small GTPases to remodel the F-actin network at sites where cells experience mechanical membrane deformations (McMahon and Boucrot, 2015). We thus examined *C. elegans* genes known to encode BAR domain proteins as well as known regulators of actomyosin network for a possible involvement in vulval lumen morphogenesis. To this aim, we performed RNAi knock-down in larvae and used, where available, mutant alleles to score lumen shape and NMY-2::GFP recruitment. The genes examined are listed in suppl. Table S1.

Through this targeted screen, we identified *toca-1* (Transducer of CDC-42 dependent actin assembly-1) and its paralog *toca-2* as regulators of lumen morphogenesis and NMY-2::GFP localization (suppl. Table S1). The *toca* genes encode two highly similar and functionally redundant F-BAR domain proteins that control actin dynamics and membrane trafficking through a CDC-42/PAR-6/WAVE pathway (Bai and Grant, 2015). In *toca-1(tm3334)* single mutant animals treated with *toca-2* RNAi or in *toca-1(tm3334); toca-2(ng11)* double mutants, the AC was able to breach the basal laminae and establish direct contact with the VulF cells, yet the lumen was abnormally shaped due to a lack of lateral constriction and dorsal lumen extension (Fig. 6A-F', suppl. Fig. S3). Moreover, the recruitment of NMY-2::GFP and F-actin to the AC-VulF contact sites was reduced in *toca-1(tm3334); toca-2(ng11)* double mutants (Fig. 6G-L).

To observe TOCA-1 localization, we generated the endogenous *gfp::toca-1(zh110)* reporter via CRISPR/CAS9 mediated recombination (Dickinson et al., 2015) (see materials and methods). GFP::TOCA-1 was expressed in both the AC and the VulF cells, where it was enriched at the AC-VulF contact sites and near the apical VulF junctions, similar to the NMY-2::GFP pattern described above (Fig. 6M-N). The displacement of the AC in *unc-6(ev400)* mutants resulted in the loss of the GFP::TOCA-1 accumulation at the AC-VulF contact sites, indicating that TOCA-1 recruitment requires physical contact between the AC and VulF cells (Fig. 6O-P). To test if the VulF membrane deformation induced by the invading AC is required for TOCA-1 recruitment, we observed GFP::TOCA-1 localization in *fos-1(ar105)* mutants. The VulF cells were not deformed on their basal side and GFP::TOCA-1 accumulation at the AC-VulF contacts sites was absent in all *fos-1(ar105)*

mutants examined (suppl. Fig. S4B-B'', n=21). Moreover, VPC-specific RNAi of *toca-1* and *toca-2* (*toca-1/-2i*) resulted in the loss of TOCA-1::GFP accumulation at the AC-VulF contact sites, while a diffuse signal persisted in the AC. (Fig. 6Q-S', 68% (n=28) of the RNAi treated animals showed a strong down-regulation of GFP::TOCA-1 in the vulval cells.) Thus, most if not all of the observed GFP::TOCA-1 accumulation at the AC-VulF contacts sites occurs in the VulF cells. Furthermore, VPC-specific *toca-1/-2* RNAi caused lumen morphogenesis defects in the affected animals, similar to those observed in the *toca-1(tm3334); toca-2(ng11)* double mutants (Fig. 6R,T, quantified in suppl. Fig. S3J).
In summary, the invading AC promotes TOCA-1 accumulation in the VulF cells to activate lateral membrane constriction. We propose that the F-BAR domain proteins TOCA-1 and TOCA-2 are used to sense the mechanical deformation of the VulF cells caused by the invading AC.

TOCA proteins induce lateral VulF constriction via the CDC-42/MRCK-1 pathway

Since TOCA proteins have been shown to control actomyosin dynamics via the CDC-42 small GTPases (Bai and Grant, 2015), we tested the role of the *C. elegans cdc-42* homolog and its downstream effectors during lateral VulF constriction. In particular, the RNAi screen described above (suppl. Table S1) identified the MRCK kinase gene *mrck-1* that acts downstream of the CDC-42 GTPase during embryonic elongation to promote actomyosin contraction by phosphorylating the myosin light chain phosphatase MEL-11 (Gally et al., 2009; Nance et al., 2005). In order to observe NMY-2::GFP recruitment specifically in the VulF cells, we made use of the $P_{egl\text{-}17}$*::nmy-2::gfp* reporter described above (Fig. 4I). RNAi knock-down of *toca-1/-2, cdc-42 or mrck-1* each caused a reduced NMY-2::GFP accumulation at the AC-VulF interface (Fig. 7A-E). Moreover, the expression of a dominant-negative mutant of *rho-1* under control of a heat-shock-inducible promoter (Canevascini et al., 2005) resulted in a reduced accumulation of NMY-2::GFP at the AC-VulF contact sites (suppl. Fig. S5 and suppl. Table S1). However, RNAi against the Rho-dependent kinase *let-502* had no effect on NMY-2::GFP localization, even though the later contraction of the vulval toroids was perturbed (suppl. Table S1) (Farooqui et al., 2012). Thus, RHO-1 may act in parallel with CDC-42 to promote lateral VulF constriction through a distinct pathway.
To determine the cellular focus of the TOCA/CDC-42/MRCK-1 pathway, we performed AC- and VPC-specific RNAi in strains carrying the *nmy-2::gfp* reporter. VPC- but not AC-specific *toca-1/-2* RNAi caused a similar mislocalization of NMY-2::GFP from the AC-VulF

contact sites, as observed in the *toca-1(tm3334); toca-2(ng11)* double mutants (Fig. 7G,J,L,O). By contrast, knock-down of *cdc-42* or *mrck-1* caused reduced NMY-2::GFP recruitment in both the VPC- and AC-specific RNAi strains (Fig. 7H-J and M-O), indicating that the CDC-42/MRCK-1 module is not only used in the VulF cells, but also in the AC. Accordingly, CDC-42 was recently shown to promote invadopdia formation in the AC, where it probably acts downstream of the UNC-40 Netrin receptor (Lohmer et al., 2016). Finally, we tested whether TOCA-1 recruitment in the VulF cells depends on CDC-42 signaling by performing AC- and VPC-specific *cdc-42* RNAi in strains carrying the GFP::TOCA-1 reporter. While AC-specific *cdc-42* RNAi resulted in the frequent loss of GFP::TOCA-1 recruitment to the AC-VulF contact sites, VPC-specific *cdc-42* RNAi did not alter GFP::TOCA-1 localization (suppl. Fig. S6).

Thus, TOCA-1 is recruited to the AC-VulF contact sites independently of CDC-42 activity in the vulval cells, suggesting that TOCA-1 acts upstream of the CDC-42/MRCK-1 pathway to induce actomyosin-driven lateral membrane constriction in the VulF cells.

DISCUSSION

Vulval morphogenesis in *C. elegans* serves as a powerful model to study how a linear array of epidermal cells forms a three-dimensional tubular organ (Schindler and Sherwood, 2012). Thanks to the relatively small number of 22 cells and recent improvements in 4D live-imaging of *C. elegans* larvae (Farooqui et al., 2012), it is possible to observe vulval morphogenesis at high spatial and temporal resolution. In this study, we have characterized the first phase of morphogenesis by observing the events that initiate the formation of the vulval lumen. We show that the invasion of the AC into the vulval epithelium controls the cell shape changes of the 1° VulF cells during lumen morphogenesis.

Sequential apical and lateral constrictions extend the lumen dorsally

Apical membrane constriction driven by actomyosin contractions initiates cell invagination in many morphogenetic processes, notably during gastrulation, neurulation and branching morphogenesis of tubular organs such as the vasculature (Sawyer et al., 2010). Apical constriction leads to cell lengthening and tissue bending, thereby initiating lumen formation. Also during vulval lumen formation, the first discernible cell shape change is the apical constriction of the two inner-most 1° VulF cells (Fig. 7P). In contrast to the above

mentioned examples, apical VulF constriction is followed by the constriction of the lateral VulF membranes. As a result of these shape changes, the vulval lumen extends dorsally towards the AC and, after the AC has fused with the utse syncytium, the vulval and uterine lumina are connected to each other. To our knowledge, vulval lumen formation is so far the only example where not only apical but also lateral constriction of the invaginating cells has been observed. Lateral and apical constriction represent two separate phases during lumen morphogenesis, as apical constriction can occur in the absence of lateral constriction, for example in *erm-1* or *fos-1* mutants. Several experiments show that the lateral VulF constriction does not simply reflect a repositioning or basal sliding of the apical junctions (Wang et al., 2012), but rather involves an actomyosin-generated force driving the contraction of the lateral cortex: (1) A relatively high tension is detectable on the lateral VulF membranes during lateral VulF constriction. (2) The basolateral actomyosin network is required to create this cortical tension. (3) F-actin is organized in a ring-shaped pattern on the lateral VulF membranes, which is characteristic of contractile membranes. (4) Lateral but not apical VulF constriction requires the formation of direct contact between the VulF cells and the AC in order to recruit the non-muscle myosin NMY-2 to the new contact site.

The transversal division of the VulE cells, which preceded the initiation of lateral VulF constriction in all our recordings, appears to coordinate the temporal sequence of apical and lateral constrictions. It is possible that the division of VulE releases tensions formed through the apical junctions between the VulF and VulE cells, thus permitting lateral VulF constriction to begin. A similar role for cell divisions in accelerating epithelial invagination has previously been proposed for tracheal placode invagination in the *Drosophila* embryo (Kondo and Hayashi, 2013). In all wild-type larvae observed, the final transversal division of VulF occurred only after the completion of lateral VulF constriction. Therefore, the coordination of vulval cell shape changes with cell divisions may establish a temporal sequence for the different morphogenetic events during lumen formation.

AC invasion induces lateral VulF constriction

The AC plays a unique role that distinguishes vulval lumen formation from other cases of tube morphogenesis. By breaching the basal laminae between the vulval cells and uterus, the AC establishes direct contact with the two VulF cells (Sherwood and Sternberg, 2003). It has previously been reported that the AC is required for the later morphogenesis of the dorsal lumen during vulval tube formation (Estes and Hanna-Rose, 2009). Our study

reveals a role of the AC at an early step of vulval morphogenesis, during the initiation of lumen formation, and provides a good rationale for the developmental timing of AC invasion. If the AC has not breached the basal laminae by the mid-L3 stage, vulval lumen formation proceeds, though at a slower speed and without lateral VulF constriction. In the absence of lateral VulF constriction, the vulval lumen does not extend dorsally and cannot be connected to the uterine lumen. The circumferential cell protrusions the AC extends towards the apical VulF junctions during the lateral constriction phase may serve as physical guides that direct the VulF cells dorsally. The loss of lateral constriction in AC ablated animals and in *fos-1* mutants indicates that the AC not only serves as guidepost but also plays an active role in inducing VulF constriction. This notion is supported by the finding that physical contact between the AC and VulF cells alters the distribution of the actomyosin network in the VulF cells at the onset of lateral constriction. The direct contact formed between the AC and VulF cells induces the recruitment of F-actin, NMY-2 and possibly also other force generators to the basal apex of the lateral membranes between the two VulF cells, thereby reorienting the contractile forces within VulF (Fig. 7P'). This mechanism involves the accumulation of the F-BAR domain protein TOCA-1 at the AC-VulF contact sites, where the basal VulF membranes are bent inward by the ventrally directed AC protrusions. F-BAR domain proteins typically form crescent-shaped oligomers that can sense membrane curvature and recruit the actin cytoskeleton to the sites of membrane deformation (Fricke et al., 2010; Salzer et al., 2017). Even though TOCA-1 is expressed in both the AC and VulF cells, the tissue-specific RNAi experiments indicate that TOCA-1 recruitment occurs predominantly on the side of the VulF cells, consistent with a role in sensing the deformation of the basal VulF surface. By contrast, the adjacent VulE cells do not undergo lateral constriction because their basal surfaces are not deformed by the AC and the VulE cells do not accumulate TOCA-1 on the apex of their lateral membranes.

Like many other F-BAR domain proteins, TOCA-1 and its functionally redundant paralog TOCA-2 contain a C-terminal SH3 domain that recruits components of the WAVE complex to regulate F-actin dynamics. During *C. elegans* embryonic morphogenesis and endocytosis in oocytes, TOCA-1 and TOCA-2 activate the CDC-42 pathway and regulate WAVE and WSP-dependent actin dynamics (Bai and Grant, 2015). We have found that during vulval morphogenesis, the TOCA proteins stabilize the actomyosin network at the contact AC-VulF sites via the CDC-42/MRCK-1 and RHO-1 pathways (Fig. 7P') (Gally et al., 2009). The highly mobile, force-generating myosin complexes are trapped once they

have reached the VulF-AC contact sites marked by the TOCA complex, where they may further stabilize F-actin bundles in a positive feedback loop. Hence, the loss of TOCA function affects both myosin and F-actin localization in the VulF cells.

There exist striking similarities between AC invasion and the invasion of metastatic tumor cells, both at the molecular and morphological level (Sherwood et al., 2005). In analogy, invasive cells do not only need to change their own shape, but they also induce cell shape changes in the tissues they invade (Blazejczyk et al., 2015). The conserved F-BAR domain proteins could play an important role in the target tissues to sense the mechanical cues generated by invading cells (McMahon and Boucrot, 2015). Such a strategy could be used by metastatic tumor cells as they move through the adjacent normal tissue and to penetrate the endothelial cell layer during intravasation (Chiang et al., 2016).

AUTHOR CONTRIBUTIONS

Q.Y., D.R., L.M. and M.D. conducted the experiments, Q.Y. and A.H. designed the experiments, analyzed the data and wrote the manuscript.

ACKNOWLEDGMENTS

We thank all present and past group members for critical discussion. We are also grateful to T. Vuong and M. Labouesse for help with the cortical tension measurements and to G. Scita for sharing the strains of *toca-1* and *toca-2* mutants the *C. elegans* Genetics Center, S. Mitani (Japan Knockout Consortium), the Gene expression consortium for providing strains, and to Andrew Fire for vectors. This research was supported by the Kanton Zürich and by grants from Swiss National Science Foundation to A.H..

REFERENCES

Andrew, D.J., and Ewald, A.J. (2010). Morphogenesis of epithelial tubes: Insights into tube formation, elongation, and elaboration. Dev Biol *341*, 34–55.

Bai, Z., and Grant, B.D. (2015). A TOCA/CDC-42/PAR/WAVE functional module required for retrograde endocytic recycling. Proc. Natl. Acad. Sci. USA *112*, E1443–E1452.

Barkoulas, M., van Zon, J.S., Milloz, J., Van Oudenaarden, A., and Félix, M.-A. (2013). Robustness and epistasis in the *C. elegans* vulval signaling network revealed by pathway dosage modulation. Dev. Cell *24*, 64–75.

Blazejczyk, A., Papiernik, D., Porshneva, K., Sadowska, J., and Wietrzyk, J. (2015). Endothelium and cancer metastasis: Perspectives for antimetastatic therapy. Pharmacol Rep *67*, 711–718.

Brenner, S. (1974). The genetics of *Caenorhabditis elegans*. Genetics *77*, 71–94.

Burdine, R., Branda, C., and Stern, M. (1998). EGL-17(FGF) expression coordinates the attraction of the migrating sex myoblasts with vulval induction in *C. elegans*. Development *125*, 1083–1093.

Canevascini, S., Marti, M., Fröhli, E., and Hajnal, A. (2005). The *Caenorhabditis elegans* homologue of the proto-oncogene ect-2 positively regulates RAS signalling during vulval development. EMBO Rep. *6*, 1169–1175.

Carpenter, A.E., Jones, T.R., Lamprecht, M.R., Clarke, C., Kang, I.H., Friman, O., Guertin, D.A., Chang, J.H., Lindquist, R.A., Moffat, J., et al. (2006). CellProfiler: image analysis software for identifying and quantifying cell phenotypes. Genome Biol *7*, R100.

Chiang, S.P.H., Cabrera, R.M., and Segall, J.E. (2016). Tumor Cell Intravasation. A Review in the Theme: Cell and Molecular Processes in Cancer Metastasis. Am. J. Physiol., Cell Physiol. *311*, C1-C14.

Dickinson, D.J., Pani, A.M., Heppert, J.K., Higgins, C.D., and Goldstein, B. (2015). Streamlined Genome Engineering with a Self-Excising Drug Selection Cassette. Genetics *200*, 1035–1049.

Dickinson, D.J., Ward, J.D., Reiner, D.J., and Goldstein, B. (2013). Engineering the *Caenorhabditis elegans* genome using Cas9-triggered homologous recombination. Nat Meth *10*, 1028–1034.

Diogon, M., Wissler, F., Quintin, S., Nagamatsu, Y., Sookhareea, S., Landmann, F., Hutter, H., Vitale, N., and Labouesse, M. (2007). The RhoGAP RGA-2 and LET-502/ROCK achieve a balance of actomyosin-dependent forces in *C. elegans* epidermis to control morphogenesis. Development *134*, 2469–2479.

Estes, K.A., and Hanna-Rose, W. (2009). The anchor cell initiates dorsal lumen formation during *C. elegans* vulval tubulogenesis. Dev Biol *328*, 297–304.

Farooqui, S., Pellegrino, M.W., Rimann, I., Morf, M.K., Müller, L., Fröhli, E., and Hajnal, A. (2012). Coordinated Lumen Contraction and Expansion during Vulval Tube

Morphogenesis in *Caenorhabditis elegans*. Dev. Cell *23*, 494–506.

Fricke, R., Gohl, C., and Bogdan, S. (2010). The F-BAR protein family Actin' on the membrane. Commun Integr Biol *3*, 89–94.

Gally, C., Wissler, F., Zahreddine, H., Quintin, S., Landmann, F., and Labouesse, M. (2009). Myosin II regulation during *C. elegans* embryonic elongation: LET-502/ROCK, MRCK-1 and PAK-1, three kinases with different roles. Development *136*, 3109–3119.

Giuliani, C., Troglio, F., Bai, Z., Patel, F.B., Zucconi, A., Malabarba, M.G., Disanza, A., Stradal, T.B., Cassata, G., Confalonieri, S., et al. (2009). Requirements for F-BAR proteins TOCA-1 and TOCA-2 in actin dynamics and membrane trafficking during *Caenorhabditis elegans* oocyte growth and embryonic epidermal morphogenesis. PLoS Genet *5*, e1000675.

Haag, A., Gutierrez, P., Bühler, A., Walser, M., Yang, Q., Langouët, M., Kradolfer, D., Fröhli, E., Herrmann, C.J., Hajnal, A., et al. (2014). An In Vivo EGF Receptor Localization Screen in *C. elegans* Identifies the Ezrin Homolog ERM-1 as a Temporal Regulator of Signaling. PLoS Genet *10*, e1004341.

Heisenberg, C.-P., and Bellaiche, Y. (2013). Forces in tissue morphogenesis and patterning. Cell *153*, 948–962.

Helker, C.S.M., Schuermann, A., Karpanen, T., Zeuschner, D., Belting, H.G., Affolter, M., Schulte-Merker, S., and Herzog, W. (2013). The zebrafish common cardinal veins develop by a novel mechanism: lumen ensheathment. Development *140*, 2776–2786.

Jaqaman, K., Loerke, D., Mettlen, M., Kuwata, H., Grinstein, S., Schmid, S.L., and Danuser, G. (2008). Robust single-particle tracking in live-cell time-lapse sequences. Nat Meth *5*, 695–702.

Kamath, R.S., Fraser, A.G., Dong, Y., Poulin, G., Durbin, R., Gotta, M., Kanapin, A., Le Bot, N., Moreno, S., Sohrmann, M., et al. (2003). Systematic functional analysis of the *Caenorhabditis elegans* genome using RNAi. Nature *421*, 231–237.

Kondo, T., and Hayashi, S. (2013). Mitotic cell rounding accelerates epithelial invagination. Nature *494*, 125–129.

Lohmer, L.L., Clay, M.R., Naegeli, K.M., Chi, Q., Ziel, J.W., Hagedorn, E.J., Park, J.E., Jayadev, R., and Sherwood, D.R. (2016). A Sensitized Screen for Genes Promoting Invadopodia Function In Vivo: CDC-42 and Rab GDI-1 Direct Distinct Aspects of Invadopodia Formation. PLoS Genet *12*, e1005786.

Lubarsky, B., and Krasnow, M.A. (2003). Tube morphogenesis: making and shaping biological tubes. Cell *112*, 19–28.

Lundquist, E., Reddien, P., Hartwieg, E., Horvitz, H., and Bargmann, C. (2001). Three *C. elegans* Rac proteins and several alternative Rac regulators control axon guidance, cell migration and apoptotic cell phagocytosis. Development *128*, 4475–4488.

Matus, D.Q., Li, X.-Y., Durbin, S., Agarwal, D., Chi, Q., Weiss, S.J., and Sherwood, D.R. (2010). In vivo identification of regulators of cell invasion across basement membranes. Science Signaling *3*, ra35.

Mayer, M., Depken, M., Bois, J.S., Jülicher, F., and Grill, S.W. (2010). Anisotropies in cortical tension reveal the physical basis of polarizing cortical flows. Nature *467*, 617–621.

McMahon, H.T., and Boucrot, E. (2015). Membrane curvature at a glance. J Cell Sci *128*, 1065–1070.

Morf, M.K., Rimann, I., Alexander, M., Roy, P., and Hajnal, A. (2013). The *Caenorhabditis elegans* homolog of the Opitz syndrome gene, madd-2/Mid1, regulates anchor cell invasion during vulval development. Dev Biol *374*, 108–114.

Nance, J., Lee, J.-Y., and Goldstein, B. (2005). Gastrulation in *C. elegans*. WormBook 1–13.

Salzer, U., Kostan, J., and Djinović-Carugo, K. (2017). Deciphering the BAR code of membrane modulators. Cell Mol Life Sci *74*, 2413–2438.

Sawyer, J.M., Harrell, J.R., Shemer, G., Sullivan-Brown, J., Roh-Johnson, M., and Goldstein, B. (2010). Apical constriction: A cell shape change that can drive morphogenesis. Dev Biol *341*, 5–19.

Schindler, A.J., and Sherwood, D.R. (2012). Morphogenesis of the *Caenorhabditis elegans* vulva. Wiley Interdiscip Rev Dev Biol *2*, 75–95.

Sharma-Kishore, R., White, J.G., Southgate, E., and Podbilewicz, B. (1999). Formation of the vulva in *Caenorhabditis elegans*: a paradigm for organogenesis. Development *126*, 691–699.

Sherwood, D.R., and Sternberg, P.W. (2003). Anchor cell invasion into the vulval epithelium in *C. elegans*. Dev. Cell *5*, 21–31.

Sherwood, D.R., Butler, J.A., Kramer, J.M., and Sternberg, P.W. (2005). FOS-1 promotes basement-membrane removal during anchor-cell invasion in *C. elegans*. Cell *121*, 951–962.

Van Fürden, D., Johnson, K., Segbert, C., and Bossinger, O. (2004). The *C. elegans* ezrin-radixin-moesin protein ERM-1 is necessary for apical junction remodelling and tubulogenesis in the intestine. Dev Biol *272*, 262–276.

Wang, Y.-C., Khan, Z., Kaschube, M., and Wieschaus, E.F. (2012). Differential positioning of adherens junctions is associated with initiation of epithelial folding. Nature *484*, 390–393.

Ziel, J.W., Hagedorn, E.J., Audhya, A., and Sherwood, D.R. (2009). UNC-6 (netrin) orients the invasive membrane of the anchor cell in *C. elegans*. Nat Cell Biol *11*, 183–189.

FIGURE LEGENDS

Fig. 1. Sequential apical and lateral constriction of VulF during during lumen formation.

(A) Schematic drawing showing the cells with the seven vulval subfates, their positions before and during lumen formation and the directions of the division axes during the last round of cell divisions. (B) Nomarski images and (B') CED-10::GFP expression during vulval invagination in a wild-type larva. See also suppl. Movie S1. For each time point, a mid-sagittal section is shown. The asterisks label the AC and the capital letters the VulF, VulE and VulD cells. (B'') Outlines of the vulval cells shown in (B') were generated with cell profiler using a custom script. The dotted circles at 140 minutes outline the dividing VulE cells, which are out of focus in the plane shown. The dashed green and red arrows indicate the constriction of the apical and lateral VulF membranes, respectively. (C) 3D reconstructions of the AC labelled with the P_{cdh3}*>mCherry::PLCδ^{PH}* reporter in magenta and the apical junctions in the vulval cells labelled with the the AJM-1::GFP reporter in green. Each panel shows an individual larva during the distinct phases of lumen formation and corresponding approximately to the time points shown in (B): Before apical constriction (0 minute in (B)), during apical constriction (40 minutes), maximal apical constriction (130 minutes), VulE division (140 minutes) and completion of lateral constriction (200 minutes). (C') Shows ventral views of the apical junctions and the rearrangement of the cells after VulE division. (C'') are single z-sections showing one of the AC protrusions towards the apical VulF junctions. The arrowheads in (C) and (C'') point at the tips of the front protrusions, the arrows indicate the contralateral protrusions. See also suppl. Movies S2 and S3. The scale bars are 5 µm.

Fig. 2. Lateral VulF constriction requires AC invasion and basolateral actomyosin.

(A) Mid-sagittal sections from 4D time-lapse recordings of the CED-10::GFP reporter in the wild-type. (A') Outlines of the vulval cells shown in (A). (B,B') A *fos-1(ar105)* mutant, (C,C') wild-type after AC ablation at the Pn.pxx stage and (D,D') an *erm-1(tm677)* mutant exhibiting reduced basolateral actomyosin localization. The asterisks label the AC and the capital letters the VulF, VulE and VulD cells. The red cross in (C) indicates the position of the ablated AC corpse. The dashed green and red arrows in the cell outlines indicate the constriction of the apical and lateral VulF membranes, respectively. For quantification, see suppl. Fig. S1. See also suppl. Movies S4 and S5. The scale bars are 5 µm.

Fig. 3. Localization of the F-actin during lumen formation.

(A) F-actin localization during vulval invagination in a wild-type larva at the Pn.pxx stage detected with the LifeAct::GFP reporter, lateral (XY) view (Farooqui et al., 2012). (A') 3D reconstruction of F-actin on the lateral VulF membrane. An anterior-posterior (yz) projection of the lateral membranes between the two VulF cells is shown. (B,B') Apical mis-localization of F-actin in *erm-1(tm677)* mutants. (C,C') Disorganized F-actin staining on the lateral VulF membranes in a *fos-1(ar105)* and (D,D') an *unc-6(ev400)* mutant larva at the Pn.pxx stage. Note the loss of the ring-shaped F-actin staining in the yz-projections in (B'), (C') and (D'). In each panel, the yellow arrowhead points at the AC-VulF contact sites. (E) Intensity plots of LifeAct::GFP along the lateral VulF membranes were generated from yz-projections as shown in the inset, using a custom script described by (Morf et al., 2013) (see also materials and methods). The error bars indicate the standard deviations and the numbers in brackets the numbers of animals analyzed. The scale bars are 5 µm.

Fig. 4. Recruitment of dynamic NMY-2 particles to AC-VulF contact sites.

(A) Time-lapse recording of an endogenous NMY-2::GFP reporter in green and the P_{cdh3}*>mCherry::PLCδ*^{PH} reporter in magenta during lateral VulF constriction. Two-channel z-stacks were recorded every 15 seconds and 3D reconstructions of selected time points are shown. See suppl. Movie S6 for the complete dataset. For each time point, the left panel shows a lateral (xy) and the right panel an anterior-posterior (zy) projection. The arrowheads point at NMY-2::GFP particles approaching the AC contact site. (B) Box plots showing the normalized diffusion coefficients of NMY-2::GFP particles that were tracked in the different regions of wild-type and *unc-6(ev400)* mutants using the µ-track software (Jaqaman et al., 2008) as outlined in suppl. Fig. S2. The numbers in brackets indicate the number of particles tracked in a total of 11 wild-type and 9 *unc-6(ev400)* recordings. The whiskers indicate the 5% and 95% percentiles. n.s., *, ** and *** indicate $p>0.05$, $p<0.05$, $p<0.01$ and $p<0.001$ in a two-tailed t-test.

(C) Localization of NMY-2::GFP in a wild-type larva at the Pn.pxx stage during vulval invagination. A lateral (XY) view is shown. (C') Anterior-posterior (yz) projection of the lateral membranes between the two VulF cells. (D-D'') Localization of NMY-2::GFP in an *erm-1* RNAi-treated larva, (E-E'') a *fos-1(ar105)* mutant and (F-F'') an *unc-6(ev400)* mutant at the Pn.px stage. Note the loss of NMY-2::GFP accumulation at the AC-VulF contact sites in the xz-projections in (D''), (E'') and (F''). (G), (H) VPC-specific and (G') (H') AC-

specific RNAi of *nmy-2* in the *nmy-2::gfp; rde-1(lf); rrf-3(lf)* background. (G) and (G') show empty vector treated controls, (H) and (H') animals treated with *nmy-2* dsRNA. Note in (H) the loss of NMY-2::GFP accumulation at the AC-VulF contact sites. (I-I'') 1° lineage-specific expression of NMY-2::GFP using the $P_{egl\text{-}17}$*::nmy-2::gfp* transgene. (I') shows a yz-projection of the lateral VulF membranes and (I'') a Nomarski image of the same animal. In each panel, the yellow arrowhead points at the AC-VulF contact sites. (J) Intensity plots of NMY-2::GFP staining along the basal VulF membranes were generated from xy-views as shown in the inset, using a custom script described by (Morf et al., 2013) (see also materials and methods). The error bars indicate the standard deviations and the numbers in brackets the numbers of animals analyzed for each genotype. The scale bars are 5 µm.

Fig. 5. Cortical tension measurements on the apical and lateral VulF membrane.

(A) Membrane recoil on the lateral VulF membrane after laser-cutting in a wild-type (top panels) and an *erm-1(tm677)* mutant larva (bottom panels) during the lateral constriction phase. The CED-10::GFP reporter was used to visualize the cell membranes. For each example, the animals are shown before (0 s) and in the first frame after the cut (0.2 s). The right panels show kymographs obtained from the recordings. The dashed red lines indicate the ventral and dorsal extent of the lateral membranes and the solid yellow lines the cutting regions. The yellow arrow in the kymographs indicates the time point of the cutting. (B) Box plots showing the average recoil velocities after lateral membrane cutting measured as described in materials and methods. (C) Apical VulF membrane recoil after laser-cutting in a wild-type (top panels) and an *erm-1(tm677)* mutant larva (bottom panels) during the apical constriction phase, as described above for (A). (D) Box plots showing the average recoil velocities after apical membrane cutting. (E) Lumen formation after cutting the lateral VulF or VulA/B membranes. The animals are shown before (0 s), immediately after (0.2 s) and 4 hours after the cut. The dashed red lines in the +4 hour panels indicate the lengths of the lateral VulF membranes after invagination. (F) Box plots showing the average length of the lateral VulF membranes measured 4 hours after cutting. The whiskers indicate the 5% and 95% percentiles, and the numbers of animals analyzed are indicated by the numbers in brackets. ** and *** indicate $p<0.01$ and $p<0.001$ determined in a two-tailed t-test. The scale bars are 5µm.

Fig. 6. The TOCA proteins are required for actomyosin driven lateral VulF constriction.

(A-C) Nomarski images and (A'-C') CED-10::GFP expression in mid-sagittal sections of wild-type and (D-F') *toca-1(tm3334); toca-2* RNAi larvae during vulval lumen formation. (A) and (D) show larvae stages before, (B) and (E) during and (C) and (F) after lateral VulF constriction. The dashed red lines in (C) and (F) indicate the lengths of the lateral VulF membranes, the white arrowheads point at the gaps in the basal laminae formed by the invading AC and the asterisks the positions of the AC. (G-G'') Localization of NMY-2::GFP in green and the P_{cdh3}*>mCherry::PLCδ^{PH}* reporter in magenta in *a* wild-type and (H-H'') a *toca-1(tm3334); toca-2(ng11)* double mutant larva at the Pn.pxx stage during vulval invagination. (G) and (H) are merged images of the mCherry::PLCδ^{PH} and NMY-2::GFP channels, (G'') and (H'') are yz-projections of the lateral VulF membranes in the animals shown in (G') and (H'). (I) Localization of the LifeAct::GFP F-actin reporter in a wild-type and (J) a *toca-1(tm3334); toca-2(ng11)* double mutant larva at the Pn.pxx stage. (I') and (J') show yz-projections of the lateral VulF membranes. In each panel, the yellow arrowhead points at the AC-VulF contact sites. (K) Intensity plots of NMY-2::GFP along the basal VulF membranes were generated from xy-views as shown in the inset and described by (Morf et al., 2013) (see also materials and methods). The error bars indicate the standard deviations and the numbers in brackets the numbers of animals analyzed for each genotype. (L) Intensity plots of Lifeact::GFP along the basal VulF membranes as described under (K). (M-N) Localization of the endogenous GFP::TOCA-1 reporter *zh110* in wild-type and (O-P) *unc-6(ev400)* mutants before (M,O) and after (N,P) lumen formation. (M', O') show yz-projections of the lateral VulF membranes.The inset in (O) shows the displaced AC in the *unc-6(ev400)* mutant in a different focal plane. (Q-T) VPC-specific RNAi in the *gfp::toca-1; rde-1(lf); rrf-3(lf)* background. (Q-R) show control animals treated with empty vector and (S-T) are *toca-1/-2* RNAi treated larvae. (Q,Q') and (S,S') show animals during constriction, (R) and (T) are Nomarski images of the stage after constriction has been completed in the wild-type (after VulE division) used for the quantification shown in suppl. Fig S3J. Note in (S) the lack of GFP::TOCA-1 accumulation at the AC-VulF contact sites and in (T) the abnormal lumen shape due to a lack of lateral VulF constriction indicated by the dashed red line. The asterisks mark the AC position and the yellow arrowheads point at the AC-VulF contact sites. The scale bars are 5 µm.

Fig. 7. A TOCA/CDC-42/MRCK-1 pathway regulates NMY-2::GFP recruitment in the VulF cells.

(A,A') P_{egl-17}*::nmy-2::gfp* larvae at the Pn.pxx stage treated with empty vector as negative control, (B,B') *toca-1/-2*, (C,C') *cdc-42* and (D,D') *mrck-1* dsRNA. (E) Penetrance of the NMY-2::GFP mislocalization phenotype observed after the different RNAi treatments. The numbers in brackets indicate the numbers of animals scored and the error bars the standard deviations estimated by bootstrapping 1000 samples. (F,F') AC-specific RNAi in *nmy-2::gfp* larvae treated with empty vector control, (G,G') *toca-1/-2*, (H,H') *cdc-42* and (I,I') *mrck-1* dsRNA. (J) Penetrance of the NMY-2::GFP mislocalization phenotype observed after different AC-specific RNAi treatments. (K,K') VPC-specific RNAi in *nmy-2::gfp* larvae treated with empty vector control, (L,L') *toca-1/-2*, (M,M') *cdc-42* and (N,N') *mrck-1* dsRNA. (O) Penetrance of the NMY-2::GFP mislocalization phenotype observed after different VPC-specific RNAi treatments. For each RNAi condition, the top panel shows an xy-view and the bottom panel a yz-projection of the lateral VulF membrane that was generated from the xy-view shown above. The yellow arrowheads point at the AC-VulF contact sites. The scale bars are 5 µm. (P) Model of the cell shape changes during the different stages of lumen morphogenesis. The cells in the images shown in Fig. 1B' undergoing apical and lateral constriction were traced using the cell profiler software package using a custom script (Carpenter et al., 2006). The basolateral membranes are shown in red and the apical membranes in blue. The division planes and directions of cell migrations are indicated with solid and dashed arrows, respectively. (P') The AC induces lateral VulF constriction by recruiting the TOCA protein complex to the AC-VulF contact sites. TOCA proteins then activate the CDC-42/MRCK-1 pathway in parallel with RHO-1 to induce actomyosin contraction.

STAR METHODS

CONTACT FOR REAGENT AND RESOURCE SHARING

Further information and requests for resources and reagents should be directed to and will be fulfilled by the Lead Contact, Alex Hajnal (alex.hajnal@imls.uzh.ch).

EXPERIMENTAL MODEL AND SUBJECT DETAILS

C. elegans *cultures*

C. elegans strains were maintained at 20°C on standard nematode growth plates as described (Brenner, 1974). The wild-type strain from which all mutant alleles used were derived is *C. elegans* Bristol, variety N2. Newly generated alleles were backcrossed at least three times against the N2 strain before analysis. In all experiments, hermaphrodite larvae were observed at the stages indicated in the figure legends.

Alleles used

LGI: *erm-1(tm677), hT2[bli-4(e937) let(q782) qIs48] (I;III)*, *nmy-2::gfp(cp13)* (Dickinson et al., 2013)*, unc-57(e406), wve-1(ok3308),* LGII: *rrf-3(pk1426),* LGIII: *toca-2(ng11)* (Giuliani et al., 2009), *abi-1(ok640),* LGIV: *srgp-1(ok300)(IV), wsp-1(gm324)(IV),* LGV: *rde-1(ne219), fos-1(ar105), nT1[qIs51, let(m435)](IV;V),* LGX: *dyn-1(ky51), unc-6(ev400)* (Ziel et al., 2009)*, toca-1(tm3334)* (Giuliani et al., 2009)*, gfp::toca-1(zh110)* (this study). Extrachromosomal and integrated arrays: *zhIs396[P_{dlg-1}>lifeact::gfp::unc-54 3'utr, P_{lin-48}>gfp]* (Farooqui et al., 2012)*, qyIs50[P_{cdh-3}>mCherry::moeABD]*, *qyIs23[P_{cdh-3}>mCherry::plc∂PH]* (Ziel et al., 2009)*, swIs79[ajm-1::gfp, P_{scm-1}::gfp, unc-119(+)]*(Diogon et al., 2007)*, qyEx19[ced-10::gfp, unc-119(+)], mfIs70[lin-31p::rde-1, myo-2p::gfp]* (Barkoulas et al., 2013)*, qyIs102[P_{fos-1a}::rde-1;myo2::yfp; unc-119]* (Matus et al., 2010), *zhEx167[hs*::*rho-1(dom.neg), sur-5::gfp]* (Canevascini et al., 2005)*, zhEx572[P_{egl-17}::nmy-2::gfp, myo-2::mcherry]* (this study).

METHOD DETAILS

Generation of endogenous gfp::toca-1 reporter

The endogenous *gfp::toca-1(zh110)* insertion was generated using the modified CRISPR/CAS9 protocol described by (Dickinson et al., 2015). The oligonucleotides used

to generate the sgRNA, the homology arms and for sequencing are listed in the key resource table. The GFP-tag was inserted at the N-terminus. *gfp::toca-1(zh110); toca-2(ng11)* double mutants show a wild-type vulval lumen morphology, indicating that the GFP::TOCA-1 fusion protein is functional.

Microscopy and image analysis

Fluorescent images and four-dimensional (4D) recording were obtained using an Olympus BX61 wide-field microscope equipped with a X-light spinning disc confocal system using a 60x Plan Apo lens and a Hamamatsu Orca Flash 4.0 CMOS camera. For the wild-type, the *erm-1* mutant and the AC ablation, we recorded five and for the *fos-1* mutant three larvae each. The graph in suppl. Fig. S1 shows the mean values ± standard deviations measured in the recordings. For 3D reconstructions, z-stacks with a step size of 0.5 µm were recorded with an Olympus FV1000 or a Zeiss LSM confocal microscope. For 4D recordings of vulval invagination, animals were mounted on 5% agarose pads containing 0.5 mM tetramisole. Images were recorded with an X-light spinning disc system at 10 minute time intervals taking 30 to 40 z-stacks with a step size of 0.3 µm per time point. The layers representing the mid sagittal sections are shown in Fig. 3 and suppl. Movies S1 & S2. Spinning disc images were processed using the Huygens Deconvolution platform (SVI) to increase the signal to noise ratio and analyzed using Fiji (ImageJ (NIH)) or Imaris (Bit-plane) software.

RNA interference

RNA interference (RNAi) was performed using the feeding method as described (Kamath et al., 2003). Briefly, P0 worms were synchronized at the L1 stage, transferred to nematode growth plates containing 3 mM IPTG and 50 ng/ml ampicillin seeded with the desired RNAi bacteria selected from the library described in Kamath et al. (2003) and allowed to grow for 5-7 days at 20°C, after which the surviving F1 progeny was analyzed.

Cell ablations experiments

Worms were mounted on 4% agarose containing 4 mM tetramisole pads for laser ablation. For cell ablations, a Leica DMLB wide-field microscope equipped with a MicroPoint Laser system using a 440nm dye cell containing 5mM coumarin that was coupled to a nitrogen laser (Photonics instruments) set at a pulse rate of 10Hz was used, as described in Farooqui et al. (2012). AC ablations were performed in late L3 larvae at the Pn.pxx stage, in which the AC had breached the basal laminae as scored with Nomarski optics. Ablated

worms were rescued from the pads and allowed to recover at 15°C for 2hours before mounting them again for 4D imaging.

Cortical tension measurements by laser nanosurgery

L4 larvae were mounted on 4% agarose pads containing 4 mM tetramisole. Cutting of the apical and lateral membranes was performed using a wavelength of 900nm using an Olympus two-photon Fluoview 1000 microscope equipped with a pre-compensated Ti:Sapphire Laser. The input power was set at 2.17± 0.05W, the length of the cutting region (yellow bars in Fig. 4) was set at around 2 µm, and the activation time was calculated by the scan speed of 1.25µs/pixel. Animals were imaged at 0.2 sec intervals with a 60x N.A. 1.1 water immersion lens before and after cutting. For each cut, we measured the maximal recoil distance between the edges of the cut membrane as indicated with the dashed red line in Fig. 4. Since the maximal recoil velocity exceeded the recording speed, we calculated the average recoil velocity as $v_{average}$= maximal recoil distance/duration of recoil (µm/sec). To quantify lateral VulF constriction after laser cutting, operated larvae were kept on the same agarose pads until the cut had been repaired as detected by the reappearance of the CED-10::GFP signal and the VulE cells had divided, when vulval lumen formation was scored (approximately 4 hours later).

QUANTIFICATION AND STATISTICAL ANALYSIS

Membrane length and intensity measurements

Measurements of apical and lateral membrane lengths were conducted on mid-sagittal sections using the measurement tools in Fiji (ImageJ (NIH)) software. The boundaries of the apical VulF membranes were defined by the AJs displaying a stronger CED-10::GFP signal. The length of the lateral VulF membranes was measured from the VulF-AC intersection to the boundary of the apical VulF membrane as shown in suppl. Fig. S1. Intensity plots of LifeAct::GFP or NMY-2::GFP along the lateral VulF membranes were generated using custom script as described (Morf et al., 2013). For each animal, the intensity in yz-axis projections of the lateral VulF membrane regions (outlined with a yellow dashed box in the example shown in the inset) or in xz-projections (blue dashed boxes) were divided into ten equal segments along the dorso-ventral axis. In each segment, the total intensity was measured and normalized to the summed intensities of all segments.

Particle tracking

The NMY-2 punctae in Fig. 4 were tracked and analyzed using the μ-track software package (Jaqaman et al., 2008). NMY-2::GFP punctae were automatically selected using a Gaussian mixture model and tracked using the motion analysis module. For each tracked particle, the normalized diffusion coefficient was calculated as a measure of its mobility.

Statistical analysis

Data were organized and analyzed using Excel (Microsoft Inc.) spreadsheets and plots were generated in Excel or using the Prism 7 (Graphpad Inc.) software package. All statistical tests such as the calculation of means, standard deviations, 95% CIs and t-tests are described in the figure legends and were performed using the built-in Microsoft Excel functions.

Supplementary Movies

Suppl. Movie S1 related to Fig. 1. Cell shape changes during vulval invagination in a wild-type larva.

Suppl. Movie S2 related to Fig. 1. Dynamic AC protrusions directed towards the AJs between the VulF cells.

Suppl. Movie S3 related to Fig. 1. 3D reconstruction of the AC protrusions and the AJs in a wild-type larva after the completion of lateral constriction.

Suppl. Movie S4 related to Fig. 2. Abnormal vulval invagination in an *erm-1(tm677)* mutant.

Suppl. Movie S5 related to Fig. 2. 3D reconstruction of the AC protrusions and the AJs in an *erm-1(tm677)* mutant failing to undergo lateral VulF constriction.

Suppl. Movie S6 related to Fig. 4. Movement of NMY-2::GFP particles along the lateral VulF cell membranes in a wild-type larva.

Suppl. Movie S7 related to Fig. 6. 3D reconstruction of the VulF cortex using the Lifeact::GFP signal in the animal shown in Fig. 3A**.** The last rotation shows a surface projection of the two VulF cells.

KEY RESOURCE TABLE

REAGENT or RESOURCE	SOURCE	IDENTIFIER
Experimental Models: Organisms/Strains		
wild-type *C. elegans*	*Caenorhabditis* Genetics Center	N2
erm-1(tm677)/hT2[bli-4(e937) let(q782) qIs48])	Haag et al. 2014	AH1890
nmy-2::gfp(cp13)	Dickinson et al., 2013	LP162
unc-57(e406)	*Caenorhabditis* Genetics Center	CB406
wve-1(ok3308)/hT2[bli-4(e937) let(q782) qIs48])	*Caenorhabditis* Genetics Center	VC2706
rrf-3(pk1426)	*Caenorhabditis* Genetics Center	NL2099
toca-2(ng11)	Giuliani et al., 2009	GU662
abi-1(ok640)	*Caenorhabditis* Genetics Center	RB829
srgp-1(ok300)	*Caenorhabditis* Genetics Center	VC202
wsp-1(gm324)	*Caenorhabditis* Genetics Center	NG324
rde-1(ne219)	*Caenorhabditis* Genetics Center	WM27
fos-1(ar105)/ nT1[sqIs51,let(m435)]	*Caenorhabditis* Genetics Center	AH1205
dyn-1(ky51)	*Caenorhabditis* Genetics Center	CX51
unc-6(ev400)	*Caenorhabditis* Genetics Center	NM434
toca-1(tm3334)	Giuliani et al., 2009	GU1165
gfp::toca-1(zh110)	this study	AH4481
zhIs396[P_{dlg-1}>lifeact::gfp::unc-54 3'utr, P_{lin-48}>gfp]	Farooqui et al., 2012	AH2453
qyIs50[P_{cdh-3}>mCherry::moeABD]	Ziel et al., 2009	NK409

qyIs23[P_{cdh-3}>mCherry::plcϑPH]	Ziel et al., 2009	NK361
swIs79[ajm-1::gfp, P_{scm-1}::gfp, unc-119(+)]	Diogon et al., 2007	SU140
qyEx19[ced-10::gfp, unc-119(+)]	Lundquist et al., 2001	AH4293
mfIs70[lin-31p::rde-1, myo-2p::gfp]	Barkoulas et al., 2013	JU2058
qyIs102[P_{fos-1a}::rde-1;myo2::yfp; unc-119]	Matus et al., 2010	NK640
zhEx167[hs::rho-1(dom.neg), sur-5::gfp]	Canevascini et al., 2005	AH995
zhEx572[P_{egl-17}::nmy-2::gfp, myo-2::mcherry]	this study	AH4720
Oligonucleotides		
toca-1 homology downstream arm forward: AGGATGACGAT GACAAGAGAAATGATAGCTGT AGTTGGGACC	this study	ODR310
toca-1 homology downstream arm reverse: aacagctatgacc atgttatATAGTGCGGCGCAAAAC CCT	this study	ODR311
toca-1 homology upstream arm forward: CAATTCTTCTCCTTTA CTCATTGTTCGCCGCTTCTTCA AAAG	this study	ODR312
toca-1 homology upstream arm reverse: acgacggccagtcgccggca CCTGGTAACCGTGAACTATAC	this study	ODR313
toca-1 sgRNA forward: cctcctattg cgagatgtcttGAATGAACGACAGT TGCAGTTGTTTAAGAGCTATG CTGG	this study	ODR321
toca-1 sgRNA reverse: CCAGC ATAGCTCTTAAACAACTGCAAC TGTCGTTCATTCaagacatctcgca ataggagg	this study	ODR320
Mutagenesis of *toca-1* sgRNA binding site: AATGAACGACAGT TGCAGTTGTTTAAGAGCTATG CTGG	this study	ODR323
Genotyping *toca-1(zh110):* CTCTTGGGAGCTACTTTTCG	this study	ODR325
Genotyping *toca-1(zh110):* CTGTGATCATGCCAGTATCAG	this study	ODR327
Recombinant DNA		
Repair template for *toca-1* CRISPR	this study	pDR19

sgRNA vector for *toca-1* CRISPR	this study	pDR20
Vulva-specific *nmy-2::gfp* expression vector	this study	pQY1

Figure 1

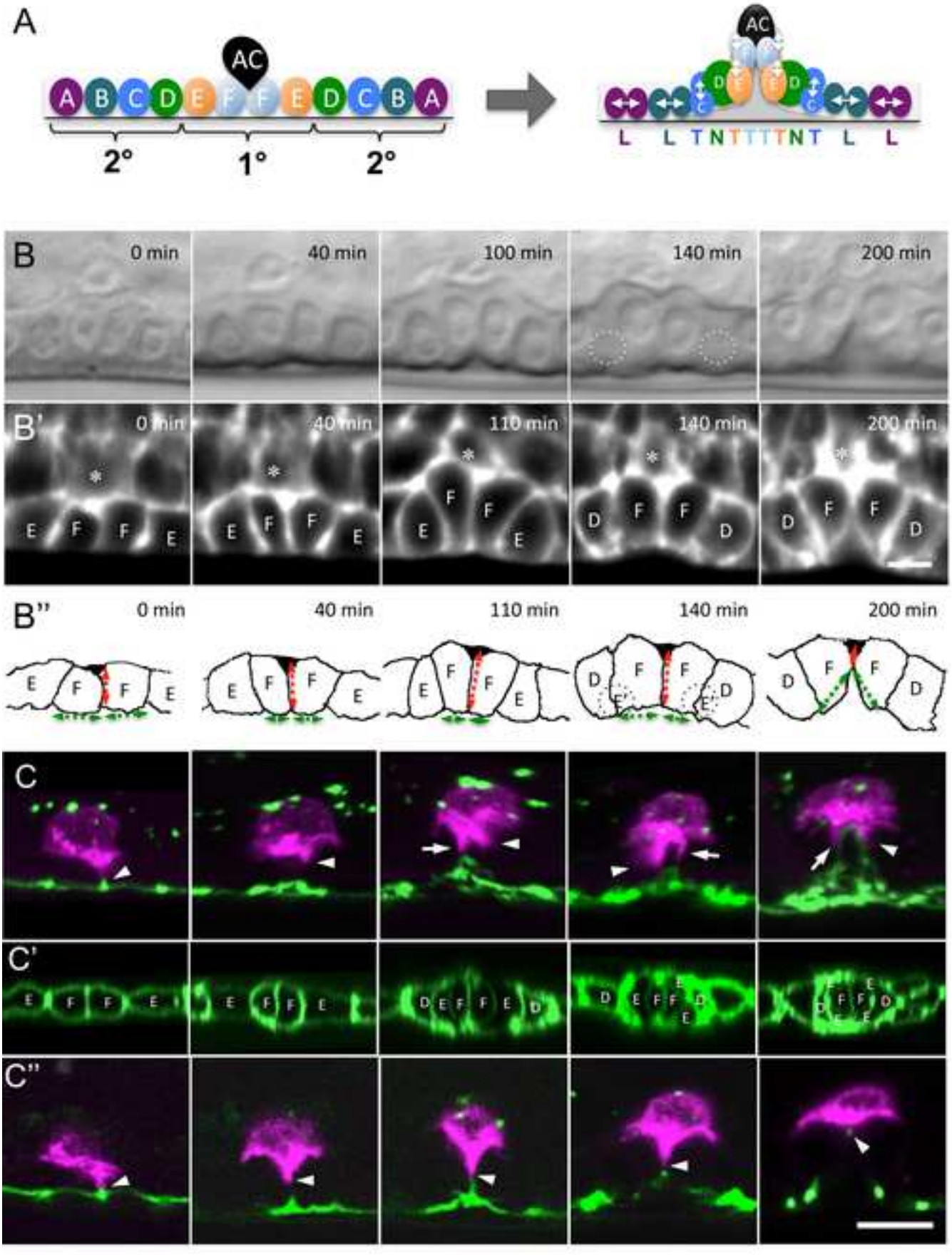

Figure 2

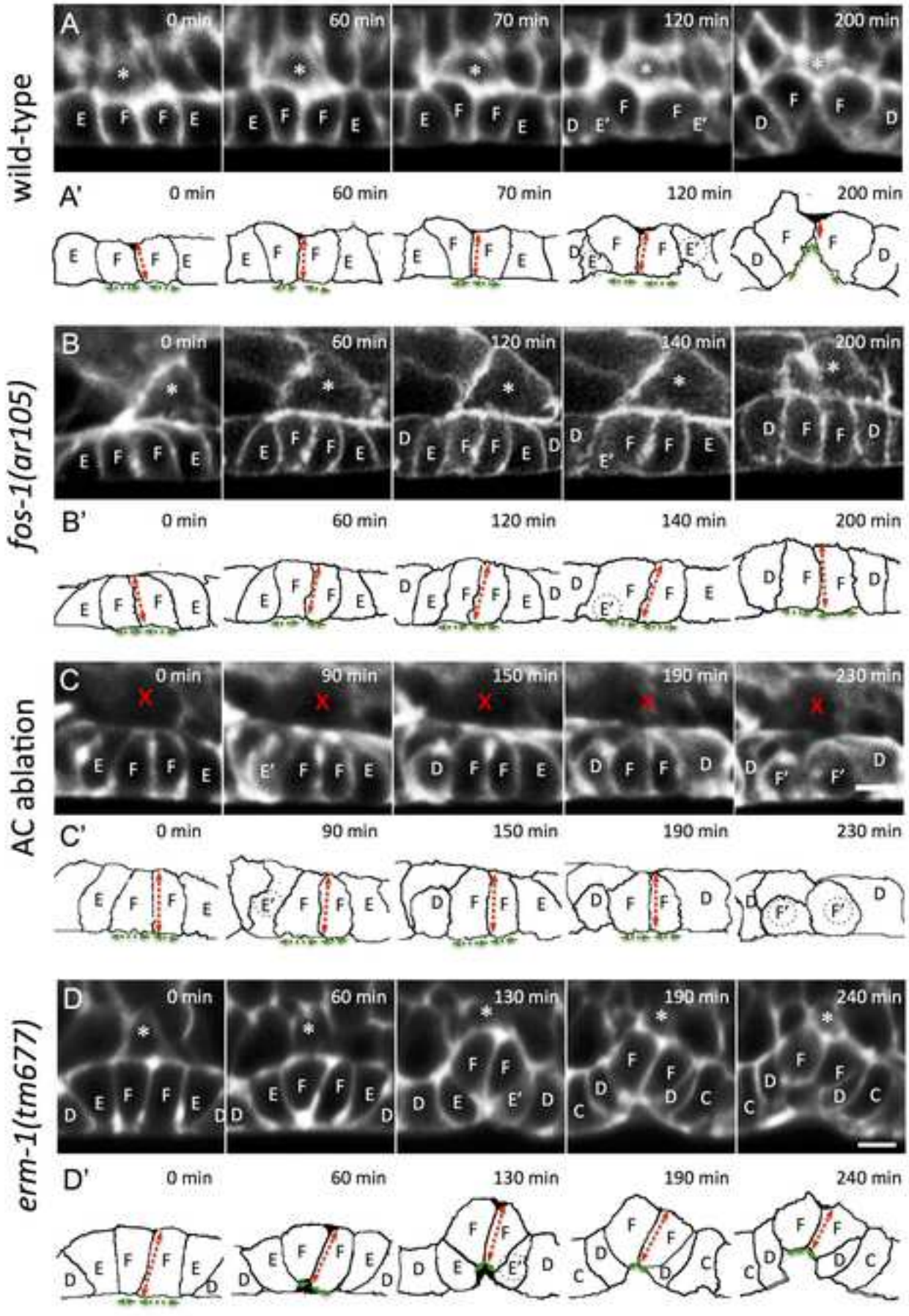

Figure 3

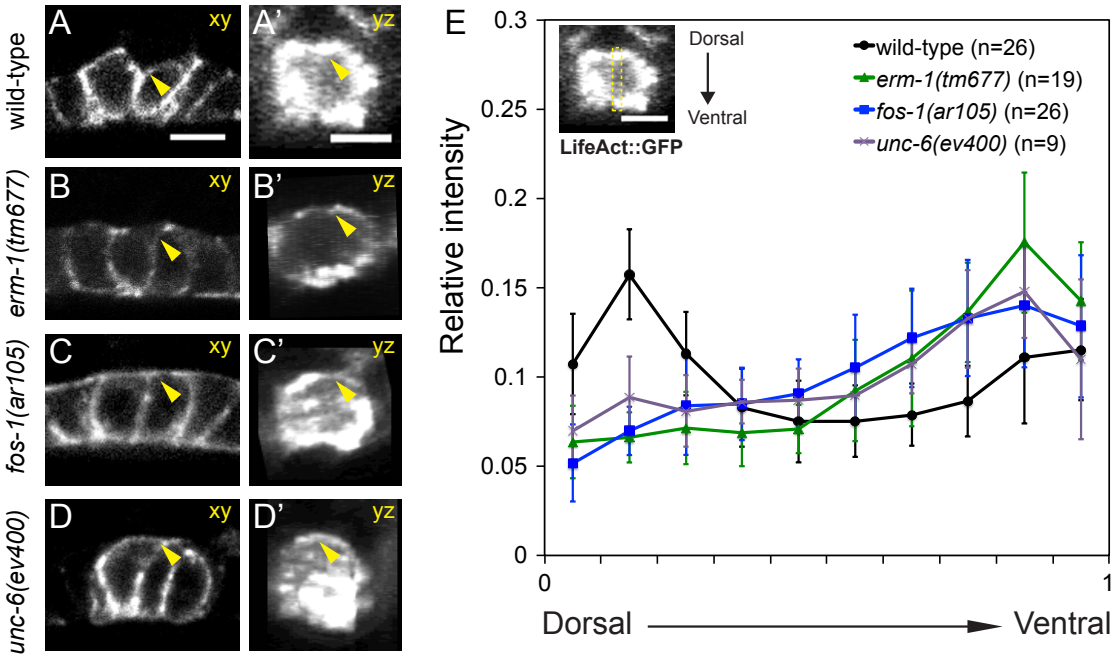
wild-type
erm-1(tm677)
fos-1(ar105)
unc-6(ev400)
A
xy
A'
yz
B
xy
B'
yz
C
xy
C'
yz
D
xy
D'
yz
E
Relative intensity
0.3
0.25
0.2
0.15
0.1
0.05
0
0
1
Dorsal
Ventral
Dorsal
Ventral
LifeAct::GFP
wild-type (n=26)
erm-1(tm677) (n=19)
fos-1(ar105) (n=26)
unc-6(ev400) (n=9)

Figure 4

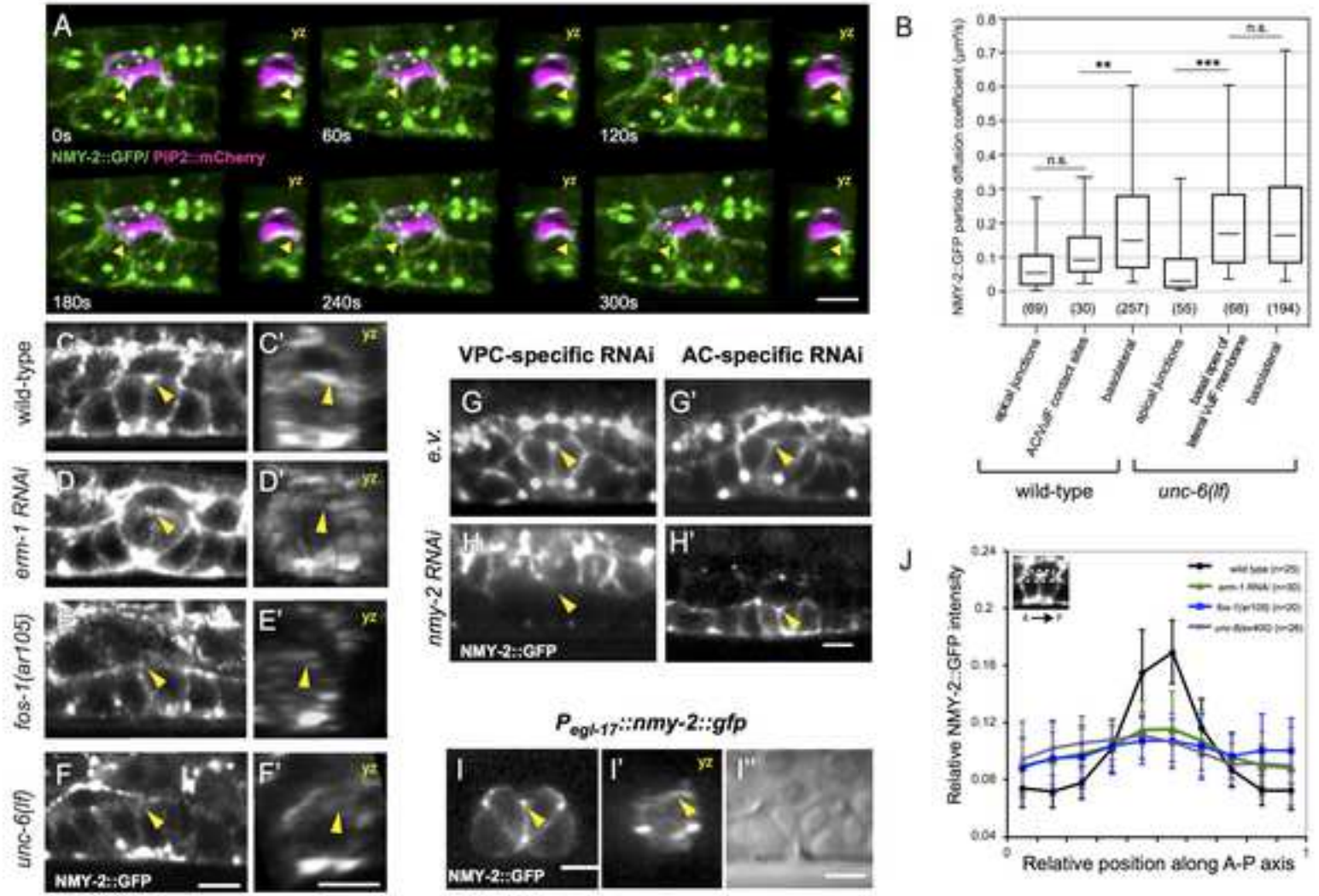

Figure 5

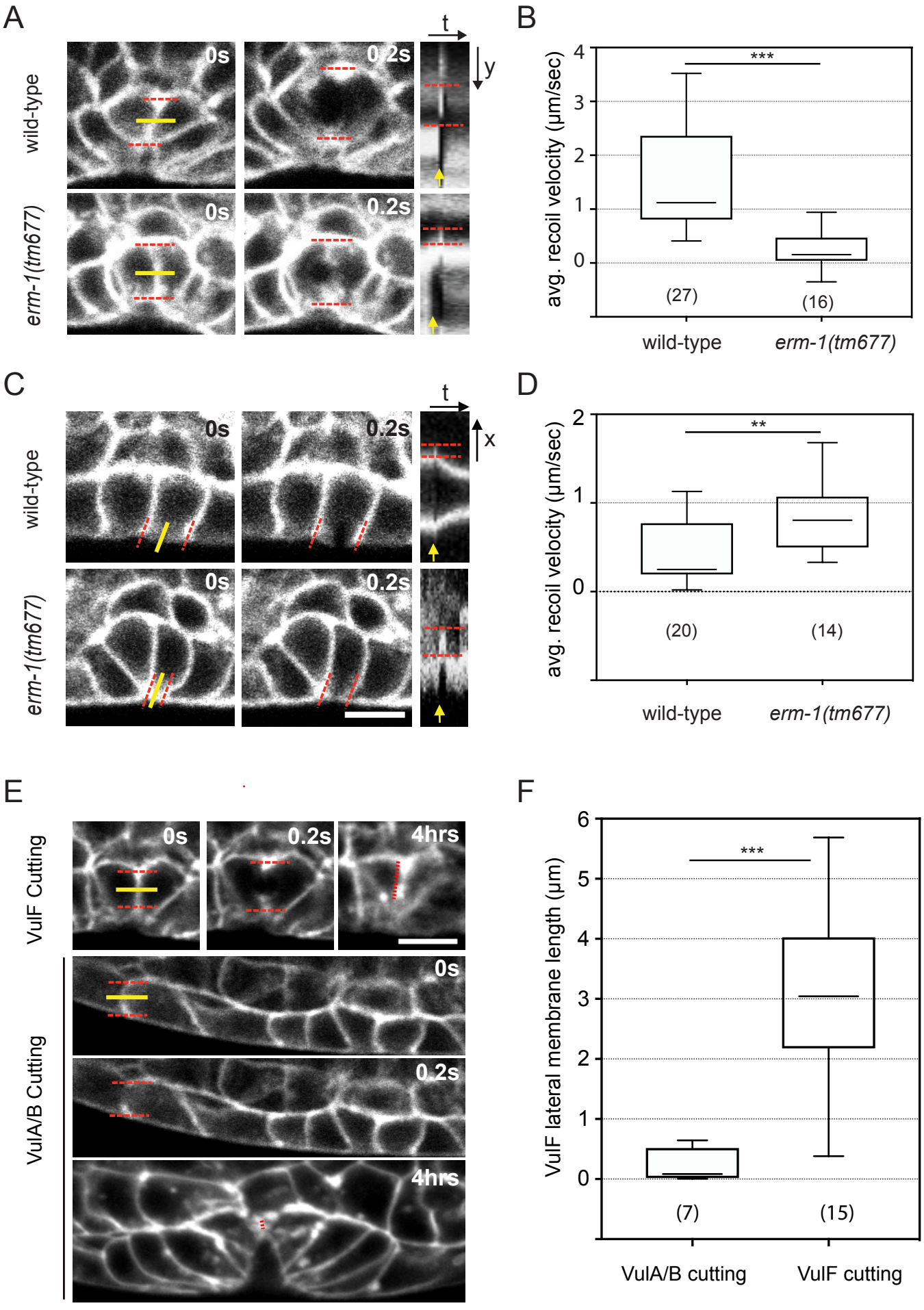
A
wild-type
erm-1(tm677)
0s
0.2s
t
y
B
avg. recoil velocity (µm/sec)
***
(27)
(16)
wild-type
erm-1(tm677)
C
wild-type
erm-1(tm677)
0s
0.2s
t
x
D
avg. recoil velocity (µm/sec)
**
(20)
(14)
wild-type
erm-1(tm677)
E
VulF Cutting
VulA/B Cutting
0s
0.2s
4hrs
F
VulF lateral membrane length (µm)
***
(7)
(15)
VulA/B cutting
VulF cutting

Figure 6

Click here to download Figure figure 6.jpg

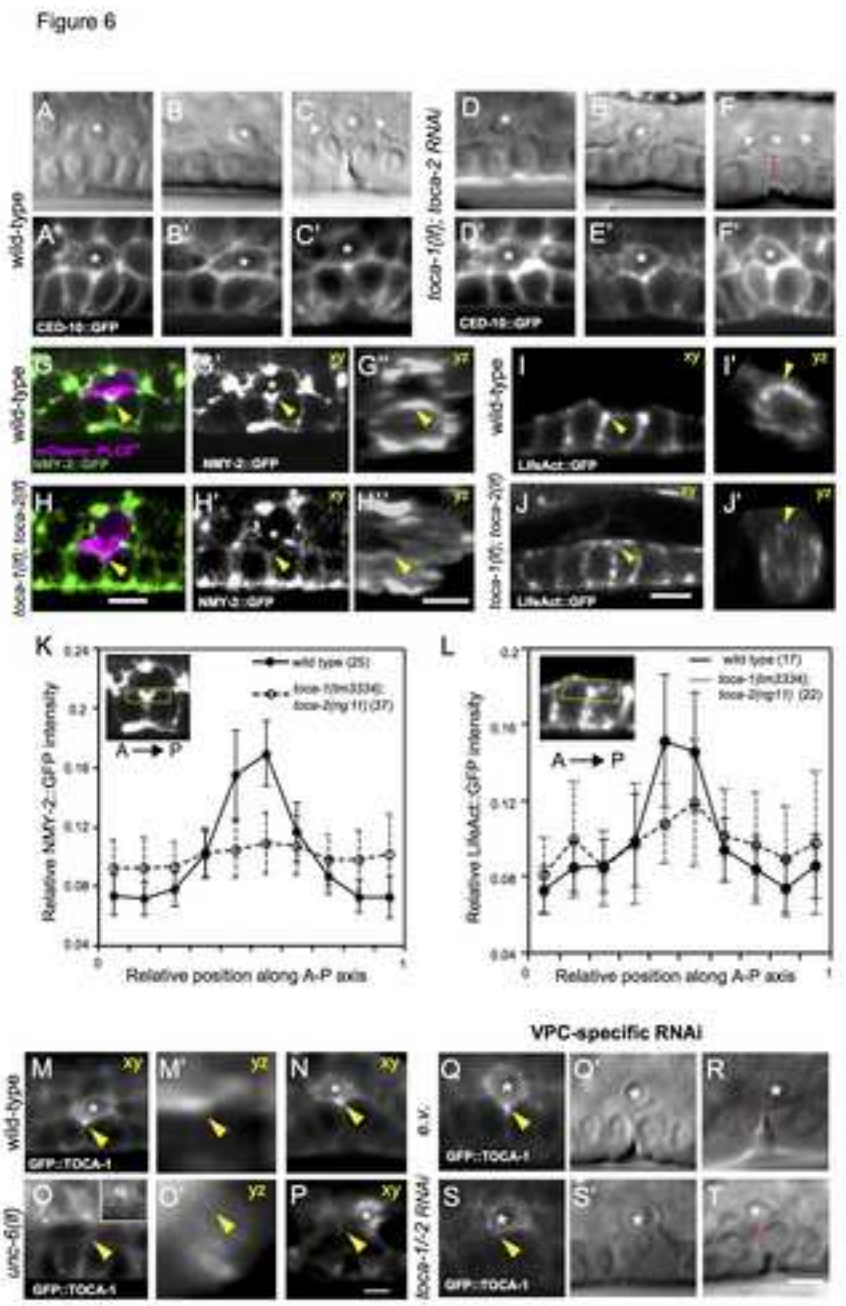

Figure 7

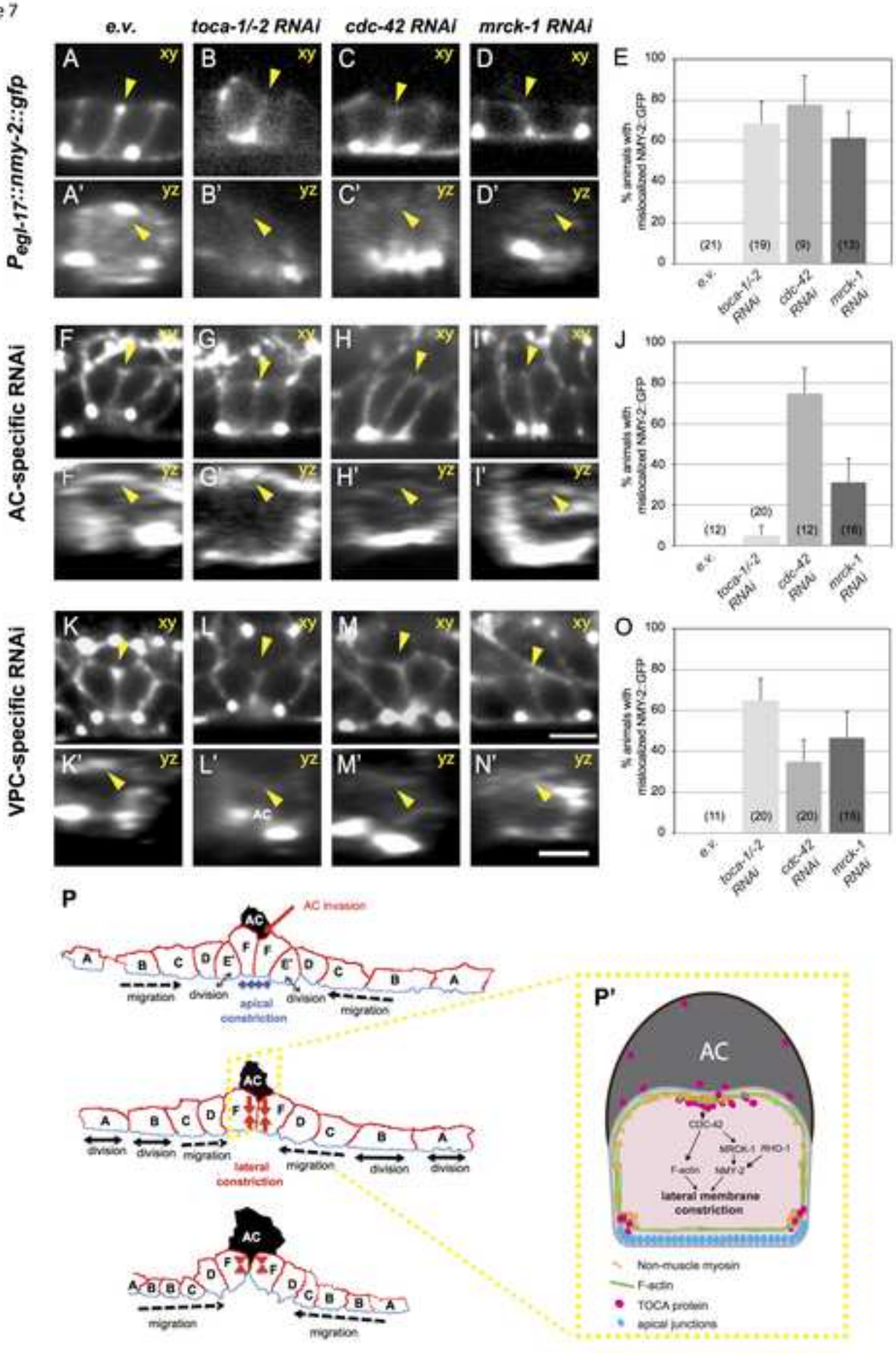

Supplementary figures

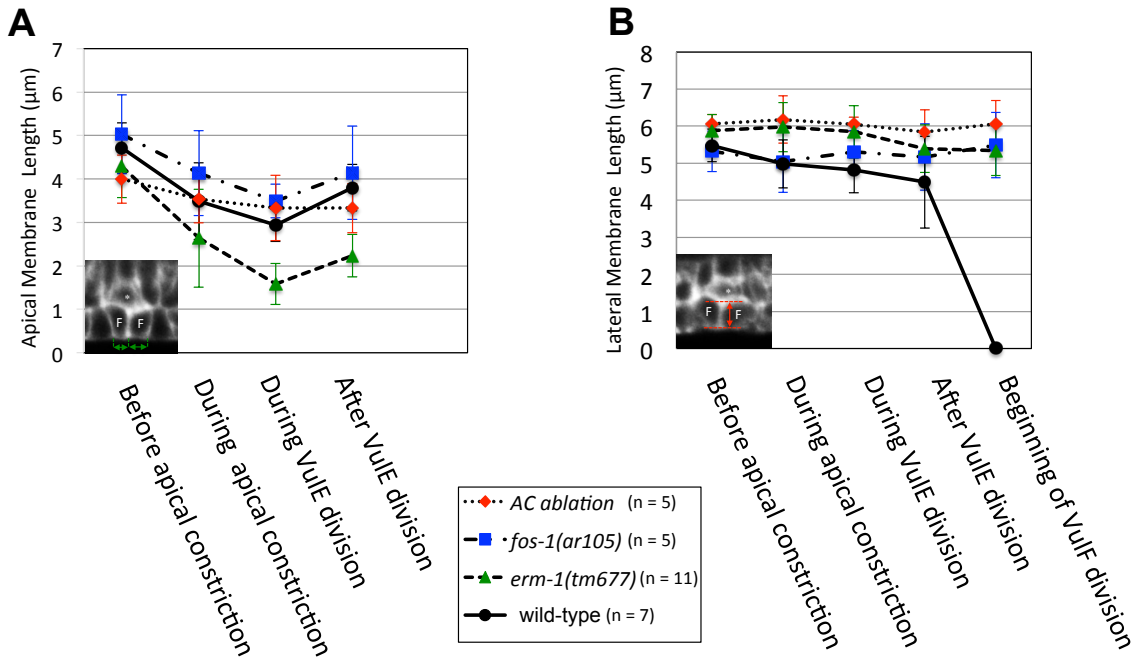

Suppl. Fig. S1 related to Fig. 2. Quantification of apical and lateral VulF membrane constriction during lumen morphogenesis.
(A) Apical cell diameters and (B) lateral membrane lengths were measured at the indicated stages as shown in the insets and described in materials and methods. Error bars indicate the standard deviations and the numbers of animals analyzed are shown in the legend.

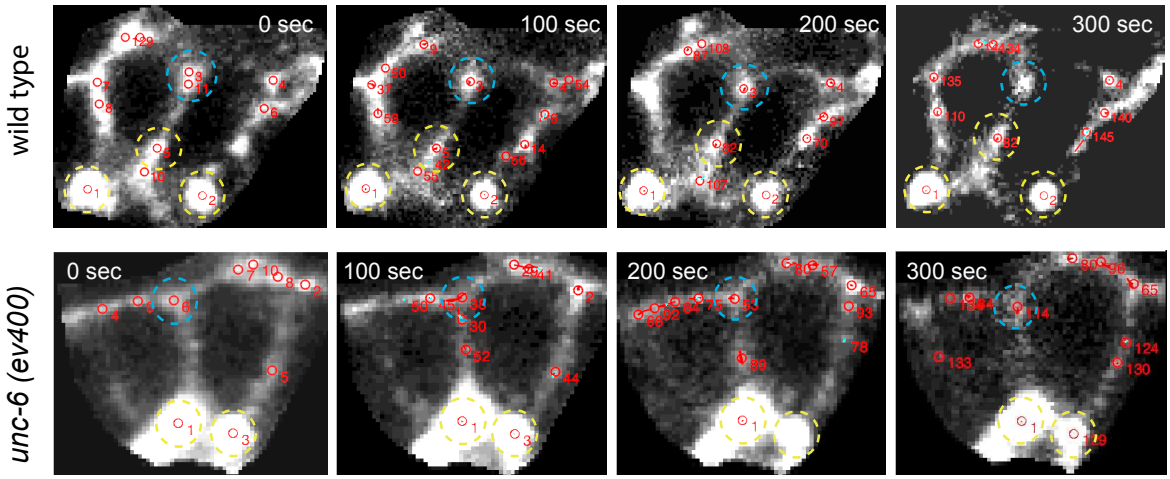

Suppl. Fig. S2 related to Fig. 4. Tracking of NMY-2::GFP particles on VulF membranes of wild-type and *unc-6(ev600)* larvae.
Mid-sagittal confocal sections of the VulF cells during lateral constriction were recorded at a one-second frame rate. NMY-2::GFP punctae were tracked and analyzed using the μ-track software package (Jaqaman et al., 2008). NMY-2::GFP punctae were automatically selected using a Gaussian mixture model and tracked using the motion analysis module. For each tracked particle, the normalized diffusion coefficient was calculated as as a measure of its mobility. Tracked punctae are marked with red circles and numbered. The yellow dashed cycles indicate the apical junctions and the blue dashed cycles the region of the AC/VulF contact sites in wild-type larvae or the basal apex of lateral VulF membranes in *unc-6(ev400)* mutants.

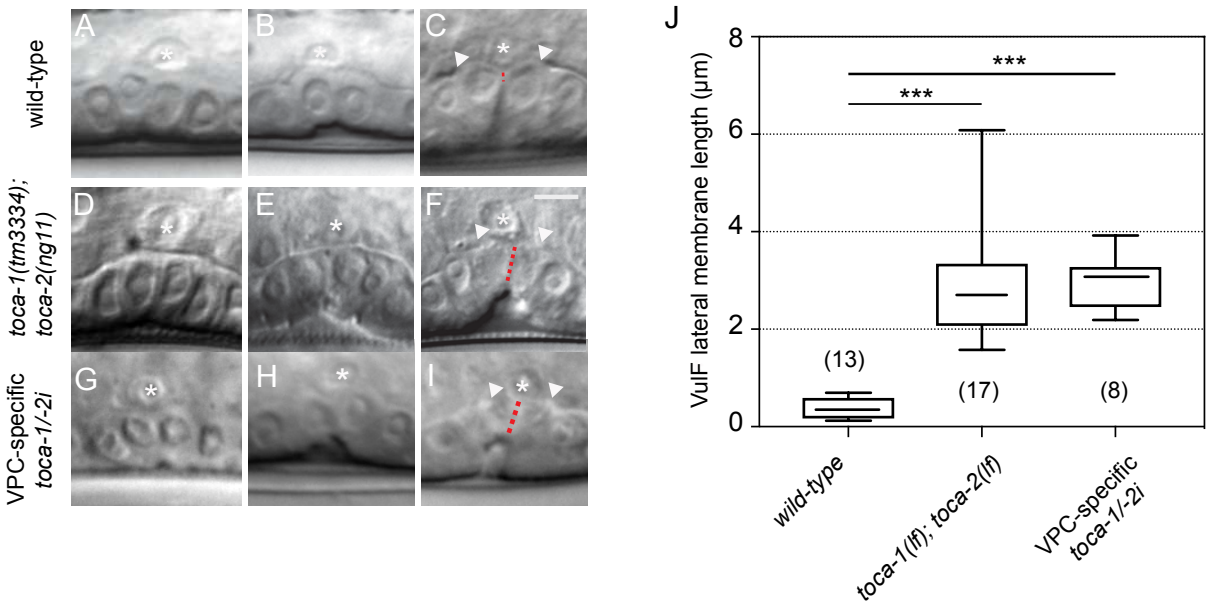

Suppl. Fig. S3 related to Fig. 6. Quantification of lateral VulF constriction in *toca* mutants and RNAi treated animals.

(A-C) Nomarski images of wild-type, (D-F) *toca-1(m3334); toca-2(ng11)* double mutants and (G-I) VPC-specific *toca-1/-2i* animals before, during and after lumen formation. The dashed red lines indicate the lateral VulF membranes and the white arrowheads the opening in the basal lamina formed by the invading AC. (J) Box plots showing the length of the lateral VulF membranes in the indicated genotypes. The whiskers indicate the 5% and 95% percentiles, and the numbers in brackets indicate the numbers of animals scored.

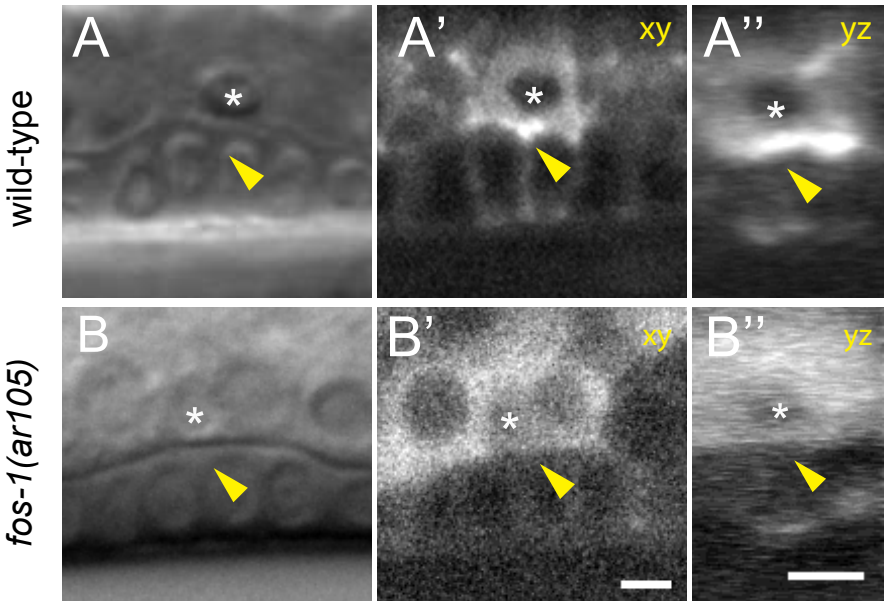

Suppl. Fig. S4 related to Fig. 6. Loss of GFP::TOCA-1 recruitment in *fos-1(ar105)* mutants.

(A) Nomarski image, (A') GFP::TOCA-1 expression in a mid-sagittal xy-section and (A'') a yz-projection in a wild-type larva at the onset of lumen formation. (B-B'') Nomarski image and GFP::TOCA-1 expression in a *fos-1(ar105)* mutant at the same stage. All of the 21 *fos-1(ar105)* larvae analyzed showed a loss of GFP::TOCA-1 recruitment to the AC-VulF contact sites. The asterisks mark the AC position and the yellow arrowheads point at the AC-VulF contact sites. The scale bars are 5 µm.

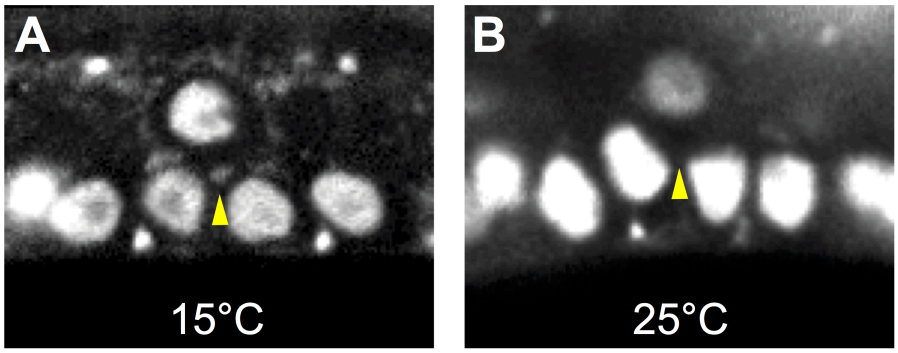

Suppl. Fig. S5 related to Fig. 7. Loss of basal NMY-2::GFP recruitment in *rho-1* dominant negative mutants.

NMY-2::GFP localization in (A) a *zhEx167[hs::rho-1(dom.neg), sur-5::gfp]* (Canevascini et al., 2005) larva grown at 15°C and (B) a larva grown at 25°C. The nuclei of the vulval and AC are labeled with SUR-5::GFP. The yellow arrowheads point at the NMY-2::GFP signal at the VulF-AC contact sites.

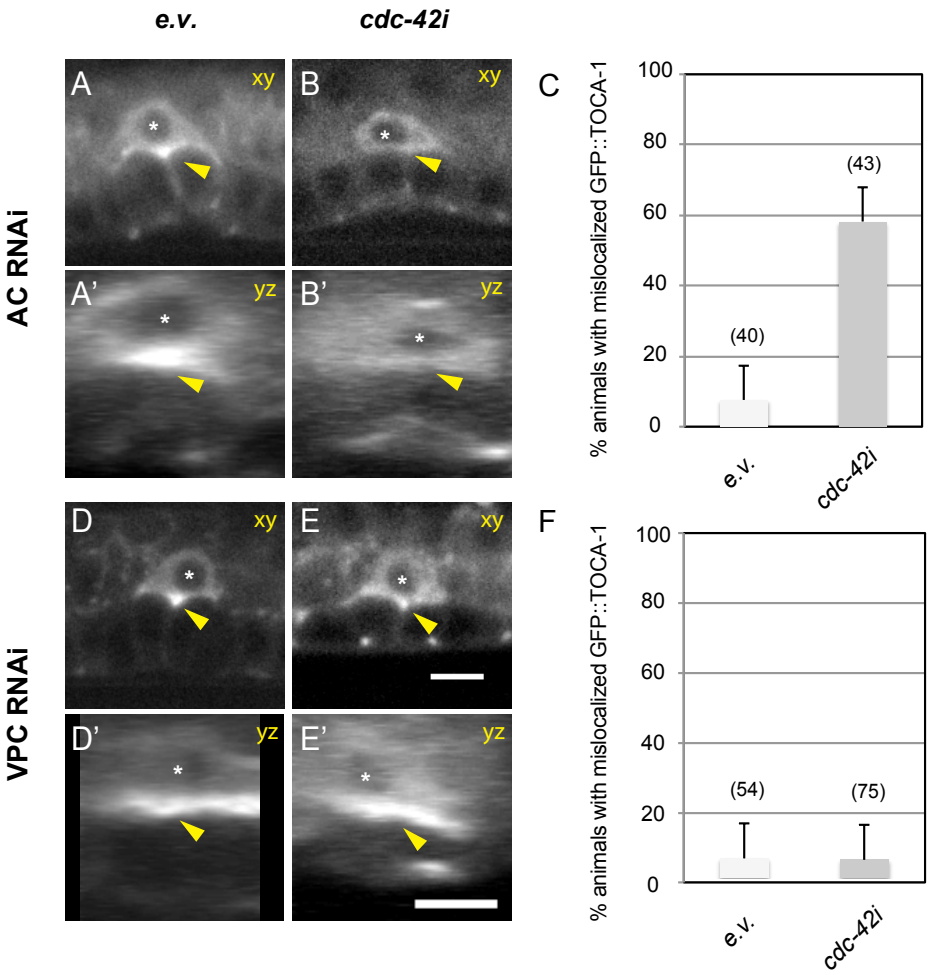

Suppl. Fig. S6 related to Fig. 7. GFP::TOCA-1 localization after AC- and VPC-specific *cdc-42* RNAi.

(A,A') AC-specific RNAi in *gfp::toca-1* larvae treated with empty vector control or (B,B') *cdc-42* dsRNA. (C) Penetrance of the GFP::TOCA-1 mislocalization phenotype observed after AC-specific *cdc-42* RNAi. (D,D') VPC-specific RNAi in *gfp::toca-1* larvae treated with empty vector control or (E,E') *cdc-42* dsRNA. (F) Penetrance of the GFP::TOCA-1 mislocalization phenotype observed after VPC-specific *cdc-42* RNAi. (A,B,D,E) show mid-sagittal xy-sections and (A',B',D',E') are yz-projections through the lateral VulF membranes. The asterisks mark the AC position and the yellow arrowheads point at the AC-VulF contact sites. The scale bars are 5 µm.

Gene name	allele or array used	RNAi clone	Brief description	Lumen shape	NMY-2 pattern
sdpn-1	-	F45E1.7	Bar-domain, synaptic dynamin binding protein	N*	N*
unc-57	*e406*	T04D1.3	endophilin A; Bar-domain protein	N	N
srgp-1	*ok300*	F12F6.5	Bar-domain, srGAP proteins	N	N
toca-1	*tm3334*	F09E10.8	Bar-domain, orthologs of human TRIP10, FNBP1L and FNBP1	**D[1]**	**D[1]**
toca-2	*ng11*	K08E3.3			
wve-1	*vc2706*	R06C1.3	WAVE protein for actin dynamic	D	N*
wsp-1	*gm324*	C07G1.4	Regulation of actin dynamic	D	N*
abi-1	*ok640*	B0336.6	Regulation of actin dynamic	N	N*
gex-3	-	F28D1.10	ligand of the small GTPase Rac1	D*	N*
arp-1	-	Y53F4B.22	ACTR1B	D*	N*
glit-1	-	F55D10.3	an ortholog of human TG (thyroglobulin)	N*	N*
par-6	-	T26E3.3	PDZ-domain-containing protein	D*	N*
mrck-1	-	K08B12.5	serine/threonine-protein kinase	**D***	**D***
let-502	-	C10H11.9	Rho-binding Ser/Thr kinase; of non-muscle myosin	D*	N*
dyn-1	*cx51*	C02C6.1	dynamin GTPase	N	N*
cdc-42	-	R07G3.1	Rho GTPase controls polarity of both individual cells	**D***	**D***
rho-1	*zhEx167 [hs::rho-1(d.neg.)]*	n.d.	Rho GTPase Regulation of actin and activation of non-muscle myosin	**D**	**D**

Suppl. Tab. S1 related to Fig. 6. List of candidate genes screened for defects in vulval lumen morphogenesis and NMY-2::GFP recruitment.

N indicates a wild-type vulval lumen and/or NMY-2::GFP localization, D indicates a defect in lumen shape and/or NMY-2::GFP localization. * Indicates that the phenotype was detected only in RNAi treated animals. [1]Only *toca-1; toca-2* double mutants exhibited the phenotype, while the RNAi clones used simultaneously interfered with *toca-1* and *toca-2*.

Supplemental Movie 1

Click here to access/download

Supplemental Movies and Spreadsheets

Movie s1.mov

Supplemental Movie 2

Click here to access/download

Supplemental Movies and Spreadsheets

movie s2.mov

Supplemental Movie 3

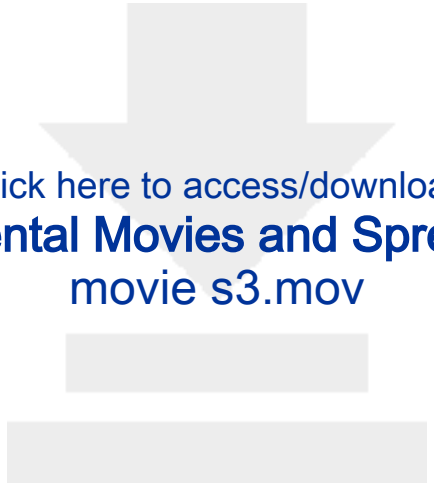

Click here to access/download

Supplemental Movies and Spreadsheets

movie s3.mov

Supplemental Movie 4

Click here to access/download

Supplemental Movies and Spreadsheets

Movie s4.mov

Supplemental Movie 5

Click here to access/download

Supplemental Movies and Spreadsheets

movie s5.mov

Supplemental Movie 6

Click here to access/download

Supplemental Movies and Spreadsheets

Movie s6.mov

Click here to access/download

Supplemental Movies and Spreadsheets

Movie s7.mov

INVENTORY OF THE SUPPLEMENTAL INFORMATION

Supplementary Figures

Suppl. Fig. S1 related to Fig. 2. Quantification of apical and lateral VulF membrane constriction during lumen morphogenesis.

Suppl. Fig. S2 related to Fig. 4. Tracking of NMY-2::GFP particles on VulF membranes.

Suppl. Fig. S3 related to Fig. 6. Quantification of lateral VulF constriction in *toca* mutants and RNAi treated animals.

Suppl. Fig. S4 related to Fig. 6. Loss of GFP::TOCA-1 recruitment in *fos-1(ar105)* mutants.

Suppl. Fig. S5 related to Fig. 7. Loss of basal NMY-2::GFP recruitment in *rho-1* dominant negative mutants.

Suppl. Fig. S6 related to Fig. 7. GFP::TOCA-1 localization after AC- and VPC-specific *cdc-42* RNAi.

Supplementary Table

Suppl. Tab. S1 related to Fig. 6. List of candidate genes screened for defects in vulval lumen morphogenesis and NMY-2::GFP recruitment.

Supplementary Movies

Suppl. Movie S1 related to Fig. 1. Cell shape changes during vulval invagination in a wild-type larva.

Suppl. Movie S2 related to Fig. 1. Dynamic AC protrusions directed towards the AJs between the VulF cells.

Suppl. Movie S3 related to Fig. 1. 3D reconstruction of the AC protrusions and the AJs in a wild-type larva after the completion of lateral constriction.

Suppl. Movie S4 related to Fig. 2. Abnormal vulval invagination in an *erm-1(tm677)* mutant.

Suppl. Movie S5 related to Fig. 2. 3D reconstruction of the AC protrusions and the AJs in an *erm-1(tm677)* mutant failing to undergo lateral VulF constriction.

Suppl. Movie S6 related to Fig. 4. Movement of NMY-2::GFP particles along the lateral VulF cell membranes in a wild-type larva.

Suppl. Movie S7 related to Fig. 6. 3D reconstruction of the VulF cortex using the Lifeact::GFP signal in the animal shown in Fig. 3A**.** The last rotation shows a surface projection of the two VulF cells.